UNIVERSITÀ DEGLI STUDI DI PADOVA

FACOLTÀ DI SCIENZE MM. FF. NN.
Dipartimento di Geoscienze
Direttore Prof. Fabrizio Nestola

TESI DI LAUREA MAGISTRALE
IN
GEOLOGIA E GEOLOGIA TECNICA

HIGH-RESOLUTION VIDEO CHARACTERISATION OF VULCANIAN PLUMES AT SABANCAYA VOLCANO, PERU

Relatore: *Prof. Andrea Marzoli[1]*
Correlatori: *Prof.ssa Costanza Bonadonna[2]*
               Dott. Paul A. Jarvis[2]
               Dott. Eduardo Rossi[2]

Laureando: Riccardo Simionato

ANNO ACCADEMICO 2020 / 2021

[1] Università degli Studi di Padova, Facoltà di Scienze MM. FF. NN., Dipartimento di Territorio e Sistemi Agro-Forestali (TeSAF) – Padova, Italy

[2] Université de Genève, Faculté des Sciences, Département des Sciences de la Terre – Geneva, Switzerland

Table of Contents

Abstract

Since November 2016, volcanic activity at Sabancaya volcano (Peru) has been characterized by multiple short-lived Vulcanian explosions per day. These Vulcanian-type explosions and related volcanic plumes were also recorded in visible light during July and August 2018.

Specific objectives of this work are to: i) develop a new algorithm to identify and isolate the plume pixels; ii) extract the main geometrical parameters of the eruptive column, such as the height and width as a function of time; iii) determine quantitative information related to the plume motion (e.g. the rise velocity and air entrainment coefficient), based on the physical quantities obtained through the first-order analysis; iv) characterize the eruption dynamics of Vulcanian plumes at Sabancaya.

The results show that the algorithm traces well the plume boundaries and is also capable of automatically calculating the geometrical parameters (height of the top, maximum width and rise velocity of the plume head). We focussed on 8 explosions that are characterized by optimal weather and plume rise conditions. The calculated height for these selected explosions ranges from 180 to 715 m within 30 seconds after ejection, while the exit velocities are up to 96.5 m/s. The air entrainment coefficients were also estimated, and lie around 0.15 ± 0.04. Moreover, we found that plumes at Sabancaya have a transient/thermal behaviour, dominated by an unsteady release of pyroclastic material that strongly controls its features and evolution.

Thus, high resolution video analysis, quantitative measurements and numerical modelling are merged here to improve the understanding of volcanic explosions at Sabancaya volcano and of volcanic plumes in general.

1. Introduction

Sabancaya volcano is an intermediate-composition stratovolcano in the Central Volcanic Zone of the Andes, situated in the Peruvian region of Arequipa. Sabancaya is the only historically active volcano of the Ampato-Sabancaya Volcanic Complex. Since November 2016, Sabancaya has been producing multiple Vulcanian explosions per day, whilst a lava dome had been concurrently growing within the crater. Vulcanian eruptions are short-lived volcanic explosions thought to result from rapid decompression of a conduit containing pressurized magma. Eruptions at Sabancaya typically have a duration from tens of seconds up to a minute and consist of a release of ash and gas, which rises as a plume to heights of 2-3 km above the vent. This work represents a multidisciplinary approach to determine eruption dynamics and physical parameters, combining high resolution video analysis, quantitative measurements and numerical modelling.

High-resolution videos of selected eruptions from Sabancaya during July and August 2018 are investigated, with the aim of extracting quantitative information on the eruption source parameters and entrainment of atmospheric air into the plumes, thus improving our understanding of the eruption dynamics. Image processing methods are used to extract geometric parameters, such as the plume height and radius as a function of time, and to provide information on turbulent structures within the plume. Various image analysis methods have been implemented using ImageJ and MATLAB to enable data extraction for variable weather conditions. A geometric calibration has also been applied to convert pixel locations into physical coordinates, considering the camera distance from the vent, orientation and inclination, as well as the local wind field.

Such a calibration allows for measurements of plume height, width and rise velocity that can be ultimately used to extract other plume and eruptive source parameters that characterize these Vulcanian eruptions. Finally, descriptions of air entrainment are made by comparing these results with experimental observations and simple theoretical descriptions with existing models from the literature.

By the end, this project is meant to help understanding the dynamics that characterize volcanic eruptions at Sabancaya by analysing high-resolution video recorded in the visible light. This is done through a semi-automatized newly developed algorithm, that represents the main aim and the most innovative part of this work. This algorithm could potentially be coupled to visible-light cameras, to be part of the monitoring network of active volcanoes. Therefore, it can hopefully be of significant use to the wide volcanological community.

This work is structured to briefly present the geology related to Sabancaya volcano and its eruptions through time up to the more recent activity, with a theoretical introduction on volcanic plumes. Then the methodology on which the algorithm is based will be presented and applied to visible light videos at Sabancaya. This will be followed by an overview of the obtained results and concluded by a final summary of the whole project.

2. Geological and Tectonic Overview

2.1. Andean Cordillera and volcanism

Located in the Southern part of Peru, almost 70 km from the city of Arequipa, Sabancaya volcano is part of the Andean Cordillera, which extends from the Caribbean area to Cape Horn along the Western side of South America. This orogen has been formed during the Early Tertiary-aged oceanic subduction of the Nazca plate beneath the South America plate; the subduction caused an uncommon and significantly thick crust (up to ~70 km) that is one of the main reasons why the origin of the Andean orogeny is still debated. The Western Cordillera in southern Peru consists of Mesozoic and Cenozoic sedimentary and volcanic formations unconformably overlying a Precambrian basement (Faccenna et al., 2017).

The geodynamic environment related to the Andean belt led to the onset of an intense and present-day lasting volcanic activity, because of the fluid-driven partial melting of the mantle wedge. This partial melting is triggered by the presence of hydrothermal fluids (e.g., released by the dehydration of the subducting oceanic crust) which act to lower the solidus and liquidus temperatures of the mantle rocks. Nowadays, the volcanic activity is focussed in three main volcanic zones: the Northern Andean Volcanic Zone (NVZ), the Central Andean Volcanic Zone (CVZ) and the Southern Andean Volcanic Zone (SVZ; for which Stern C. R. (2004) further distinguished its southern-most part as the Austral Andean Volcanic Zone, AVZ). Each one of these volcanic zones, is interspersed from the others through active-volcano-free regions that are due to the presence of flat-slab subduction zones and are referred to as flat-slab segments. The only exception is the AVZ which is separated from the SVZ by the Patagonian Volcanic Gap. It is important to notice that these regions of no activity have exhibited volcanic activity in the past but not in the Quaternary. In contrast to more-typical subduction zones, in which the slab plunges directly into the Earth's mantle at a certain angle, in flat-slab subduction
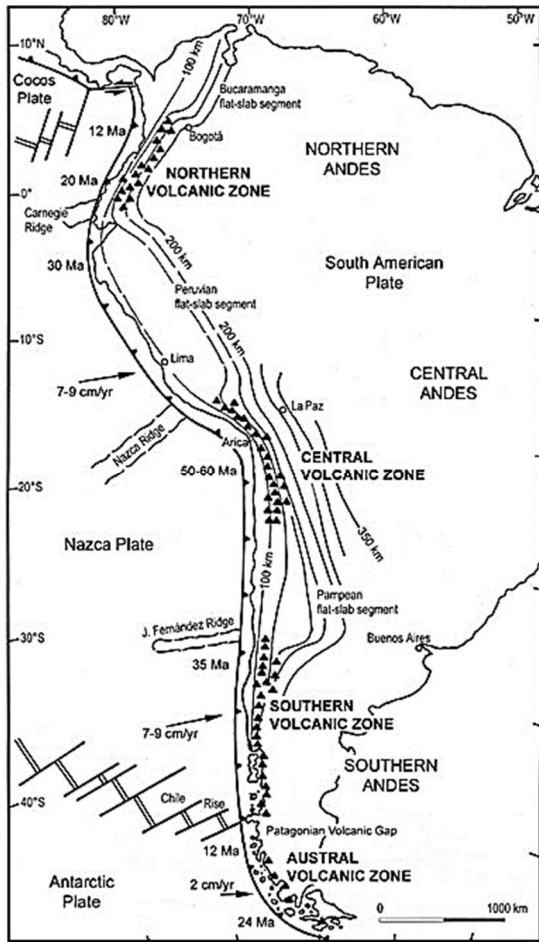
Fig. 1.1: Schematic map of South America and the Pacific oceanic plates, showing the volcanically active segments in the Andes (Stern, 2004).
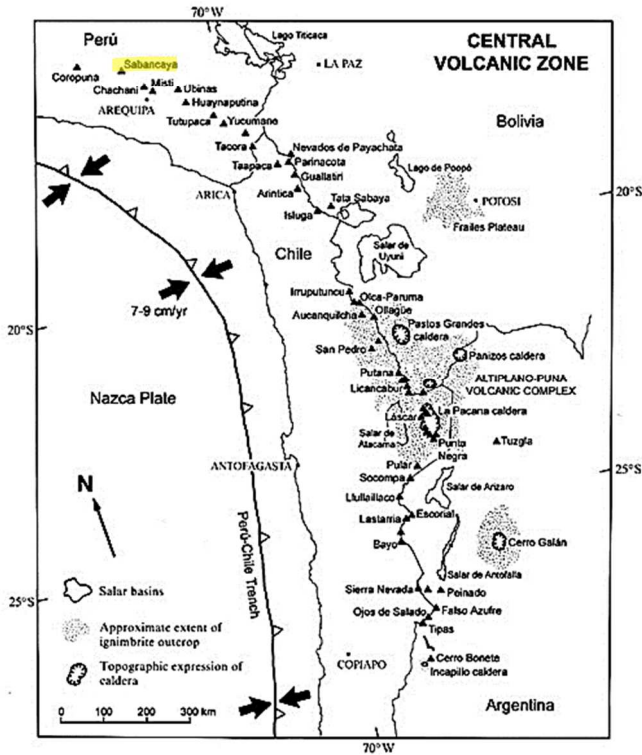

Fig. 1.2: Schematic map of the Central Andean Volcanic Zone, showing the location of some of the better-known volcanoes and caldera systems. Sabancaya volcano can be found on the top (Stern, 2004).

zones, after an initial normally-dipping portion, the slab moves horizontally for several hundreds of kilometres before sinking into the mantle (Lim et al., 2018; Manaea et al., 2017; Stern, 2004).

In this framework, the CVZ includes 44 active volcanic edifices (6 of which are in Peru) and is bordered by the Peruvian flat-slab segment to the north and by the Pampean flat-slab segment to the south. One of the more active volcanic centres in the CVZ is Sabancaya volcano, Peru, which is the subject of this thesis.

2.2. Sabancaya volcano

Sabancaya is an intermediate-composition stratovolcano belonging to the Ampato-Sabancaya Volcanic Complex (ASVC). The ASVC lies to the south of an inactive and erosion-undergoing stratovolcano, named Hualca Hualca. Hualca Hualca is the oldest stratovolcano in this area and was probably constructed during the late Pliocene and early Pleistocene. The ASVC stands on an Upper Neogene volcanic plateau and consists of Ampato volcano (to the south) and Sabancaya volcano (to the north, bordering with Hualca Hualca volcano), that is also the youngest and only active volcano of the complex (Mariño et al., 2016; Rivera et al., 2016).

2.2.1. Morphology

The summit of Sabancaya volcano is at a height of 5980 m above sea level, while the whole volcanic edifice covers a 65 to 70 km^2 area and represent a 6 to 7 km^3 volume. The edifice consists of double conical-shaped structures built up by alternating layers of lava and tephra, aligned towards a SW-NE direction. The older cone is located south-westward (towards Ampato volcano) and presents a circular lava dome on the top, whereas the younger one contains the active crater of the volcano. The northern stratocone is approximately 800 m high from the volcano base level, represented by subhorizontal lavas. This part of the edifice can be subdivided into two main zones: a lower semi-flat area of rough surfaces (10-15°); and an upper area with steeper slopes (20-45°), made up of inclined lava flows and

covered by ash (linked to the 1988-1998 activity). The semicircular active crater has a 300 m median diameter (384 m at the maximum) and a depth that can easily reach 200 meters. Moreover, based on the lava flows and the small dome mapped during various geological surveys, the presence of two more emission centres in the proximity of the main crater (within a 3.5 km radius) was inferred (Rivera et al., 2016).

Sabancaya volcano has not been affected by glacial activity during the Last Glacial Maximum (LGM). Thus, the morphology of Sabancaya, slightly eroded and without remarks of glacial activity, suggests a more recent growth than Hualca Hualca and Ampato volcanoes, that possibly took place during the Holocene (Rivera et al., 2016).

Fig. 1.3: Photo of the ASVC from the Lluillipampa area (Rivera et al. 2016).

Fig. 1.4: Photo of the active crater taken in 2011 from the top of the cone (Rivera et al. 2016).

2.2.2. *Stratigraphy*

As already mentioned, Sabancaya volcano is the youngest volcano of the ASVC, as determined by observations during geological surveys of the deposition and distribution of volcanic deposits and the interpretation of aerial and satellite imagery. Moreover, lava and ash deposits suggest construction lasted from 10000-6000 years ago until 3000 years ago (Rivera et al., 2016).

The geological units forming the substrate below Sabancaya are voluminous pyroclastic flow deposits (ignimbrites), volcanoclastic deposits and andesitic-to-dacitic lava flows. These volcanic sequences derive from the oldest volcanoes of the area (e.g., Ampato, Hualca Hualca, Ananta, Patapampa, Ampi and Jollo Jello) and overlie the older Precambrian basement and the Mesozoic-Cenozoic sequences. Dating of these deposits gives a range between Upper Miocene and Pleistocene (Mariño et al., 2016; Rivera et al., 2016).

The following discussion on the stratigraphy of the Sabancaya volcano area will also consist of a description of the building phases of the edifice (Rivera et al., 2016; Samaniego et al., 2016), as this volcano has been characterised by a dichotomy between effusive eruptions producing blocky lava flows and low-to-moderate explosive activity (Fig. 1.5). Geological investigations show that Sabancaya volcano was built in three different stages, named «Sabancaya I», «Sabancaya II» and «Sabancaya III». During the «Sabancaya I» stage, blocky lava flows of andesitic and dacitic composition were emplaced, directly in contact with the lavas and volcanoclastics of the plateau. Nowadays, these lavas constitute the foot of the volcano, and are characterized by a silica range between 61-65 wt. %, a porphyritic texture with a mineral composition including phenocrystals of plagioclase, amphibole, biotite, pyroxene and Fe-Ti oxides, and can reach up to 7 km from the emission centre (mainly because of the topography of the area and physical properties of the magma). When the chemical composition is closer to a dacite, the main effects on the rock are a greater proportion of biotite and a reduction in pyroxene with respect to the andesites. These features are almost constant in all the later lava flows emitted by Sabancaya volcano, thus must be considered valid if
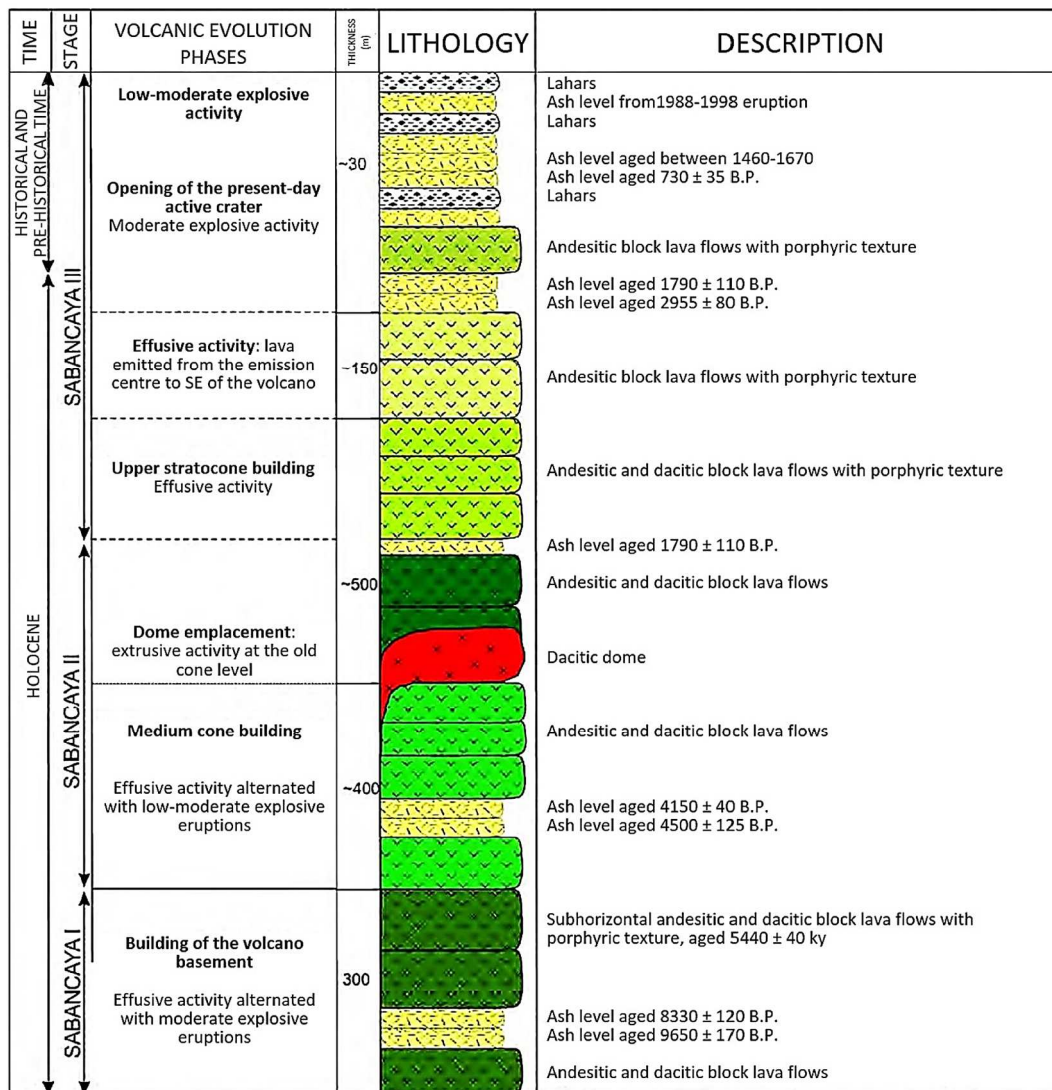
TIME	STAGE	VOLCANIC EVOLUTION PHASES	THICKNESS (m)	LITHOLOGY	DESCRIPTION
HISTORICAL AND PRE-HISTORICAL TIME	SABANCAYA III	Low-moderate explosive activity	~30		Lahars / Ash level from1988-1998 eruption / Lahars
		Opening of the present-day active crater / Moderate explosive activity			Ash level aged between 1460-1670 / Ash level aged 730 ± 35 B.P. / Lahars / Andesitic block lava flows with porphyric texture / Ash level aged 1790 ± 110 B.P. / Ash level aged 2955 ± 80 B.P.
HOLOCENE		Effusive activity: lava emitted from the emission centre to SE of the volcano	~150		Andesitic block lava flows with porphyric texture
		Upper stratocone building / Effusive activity			Andesitic and dacitic block lava flows with porphyric texture / Ash level aged 1790 ± 110 B.P.
	SABANCAYA II	Dome emplacement: extrusive activity at the old cone level	~500		Andesitic and dacitic block lava flows / Dacitic dome
		Medium cone building	~400		Andesitic and dacitic block lava flows / Ash level aged 4150 ± 40 B.P. / Ash level aged 4500 ± 125 B.P.
		Effusive activity alternated with low-moderate explosive eruptions			
	SABANCAYA I	Building of the volcano basement	300		Subhorizontal andesitic and dacitic block lava flows with porphyric texture, aged 5440 ± 40 ky
		Effusive activity alternated with moderate explosive eruptions			Ash level aged 8330 ± 120 B.P. / Ash level aged 9650 ± 170 B.P. / Andesitic and dacitic block lava flows

Fig 1.5: Lithostratigraphic column presenting Sabancaya volcano stratigraphy (modified from Rivera et al. 2016).

there are not further descriptions. Moreover, already from this first stage, some ash fallout deposits interlayer the lava flows, clearly showing that the effusive activity was alternated with low-to-moderate explosions. Similarly, «Sabancaya II» stage is characterized by andesitic-to-dacitic blocky lava flows overlying the earlier lavas of «Sabancaya I» with ash levels in between. In the same period, the emplacement of an andesitic lava dome happened. This structure can be observed to the south of the active crater of Sabancaya and cuts the «Sabancaya II» lavas. According to some authors, these two stages can be merged as they result in the development of the basal edifice of the volcano. The last stage of the formation of

16

the volcano – «Sabancaya III» – is characterized by the formation of the upper part of the edifice by andesitic blocky lava flows (dacitic composition is slightly represented), by effusive activity from an adventitious crater producing a subhorizontal andesitic blocky lava flow and by the opening of the crater still active today. As these lavas are channelized into a glacial valley (even though Sabancaya volcano was only slightly affected by glacial erosion), they can easily be defined as Holocene-aged. After the opening of the crater, moderate magnitude explosive eruptions emitted ash deposits and bombs, contributing to create the ash cone that lies on top of Sabancaya lava flows. This activity was dated as occurring in the last 1000 years.

Other geomorphological elements can be found near to Sabancaya volcano are moraines that have been related to different periods: LGM moraines outcropping at the base of the ASVC (25-17 ky), moraines associated with a late glacier re-advance (10-13 ky) and younger small moraines related to Holocene fluctuations (Rivera et al., 2016).

2.2.3. *Regional and local tectonic structures, deformation, and seismicity*

The ASVC is located within a complex tectonic environment, expressed by the presence of different types of faults, fractures and lineaments, of different scale and direction. In fact, structural systems can range from regional to local extent, with four preferential strikes (NW-SE, E-W, N-S, NE-SW). Among these, only the NW-SE, E-W and NE-SW sets are seismically active. The NW-SE faults are characterized by sinistral oblique-slip extensional dynamics. The E-W set, with a southward normal dip-slip component, is perpendicular to the overall direction of shortening in the arc, and this could be due to the collapse of the highest-elevation regions of the Andes, in which the compressive stresses causing thrust faulting in the lowlands are insufficient to support the highest-elevation mountains. The third faulting system is composed of NE-SW striking faults representing local extensional structures. These latter structure seem to be the focus of several seismic

events that have occurred during the last few decades (Rivera et al., 2016; Samaniego et al., 2016).

The local faulting systems are supposed to play a relevant role in the magma ascent as they are the main pathways responsible of the rise of the magma from the magma chamber to the conduit to produce eruptions and high degassing (Moussallam et al., 2017). This is strongly evidenced at Sabancaya volcano as a number of interferometric studies related to the 1990-1998 eruption agree that the main magma chamber is located just below Hualca Hualca volcano, at a minimum depth of 12 kilometres (Boixart et al., 2020; Jay et al., 2015; Pritchard & Simons, 2004). Thus, the magma should move through a permeable network of fractures. However, subsidence directly associated with eruptions at Sabancaya has not been observed. Thus, it could have been masked by simultaneous inflation in the magma chamber and by the fact that single eruptive episodes at Sabancaya usually do not involve large amounts of magma (Pritchard & Simmons, 2004). Moreover, mafic recharge at depth destabilizes the magmatic plumbing system, pushing it towards eruption and causing static stress transfer from the inflation that drives creep and pushes faults closer to failure. This can also be helped by extensive hydrothermal activity and high pore fluid pressures, possibly explaining why larger earthquakes can be observed at Sabancaya than at others volcanoes (MacQueen et al., 2020).

3. Eruptions at Sabancaya through time

During the last few thousand years, Sabancaya volcano has been characterized by low-to-moderate explosive activity (Volcanic Explosivity Index, VEI, of 1-2) which produced mainly andesitic ash emissions, as constrained from the study of nearby deposits. Late Holocene tephrochronology reveals recurrent explosive activity, with at least 7–9 eruptions during the last 4000–5000 years, including the historic eruptive phase of the 17th–18th century, the eruptive episode at the end of the 20th century and the activity still ongoing at the time of writing. However, even if Sabancaya's historical eruptive activity is not well described in the scientific literature, its Quechua name «Sahuancqueya», meaning volcano that spits, is very emblematic and signifies that the eruptive behaviour today is probably similar to that of the past. In fact, just considering the above-mentioned eruptive phases, based on their description and on their related deposits, they seem to be quite similar in their development, since they all present Vulcanian and phreatomagmatic activity (mainly because of the presence of an ice cap on the top of the volcano, that also triggered lahars) accompanied by tephra emissions (Mariño et al., 2016; Rivera et al., 2016).

Vulcanian eruptions are short-lived volcanic explosions, generally described as VEI 2-3, thought to result from rapid decompression of a conduit containing pressurized magma. They are driven by the accumulation of gas below a weakly-permeable or impermeable plug of degassed crystalline magma until the gas pressure is capable of fracturing the plug, thus initiating the eruption (Sigurdsson et al., 2015).

3.1. Historically-recorded eruptions

The first occidental written records of Sabancaya's activity can be found in 1750 in the writings of the priest of Salamanca. According to this witness, the volcano was «perennially burning day and night and that there is no news of having caused damages during the time of Christianity, although there is no lack of signs of to

have erupted its harshness in unmemorable times». As also supported by field evidence, this would have been a weakly-explosive eruption and may have been associated with small local ash deposits (Mariño et al., 2016; Rivera et al., 2016).

The activity of 1784–85 is also mentioned in Spanish chronicles, testifying that small-entity volcanic activity, following by some months the huge earthquake that devasted the city of Arequipa, happened (Rivera et al., 2016; Samaniego et al., 2016).

Then, for almost 200 years, Sabancaya experienced a period of quiescence characterised by low fumarolic activity. This phase ended in 1986 when frequent vapour and minor ash emission were reported, and intense fumarolic activity resulted in gas plume heights of 100s m. The surface activity and seismicity gradually increased, eventually becoming explosive in May 1990, with up to 50 events per day in the following months (VEI 2-3). Explosive activity lasted for eight years, being especially intense from 1990 to 1992 with an average of one explosion every 20-30 minutes, lasting at least one minute and producing 3-4 km-high plumes (with a maximum of 7 km) and ash falling as far as 12 km away from the volcano summit. The 1990–1998 eruptive activity consisted of alternating Vulcanian and phreatomagmatic to phreatic events (Gerbe & Thouret, 2004; Mariño et al., 2016; Rivera et al., 2016). A classical model to describe Vulcanian eruptions implies gas overpressurization within the magmatic system, caused by the cooling and crystallization of mainly anhydrous minerals, leads to rock fracturing and eruptions (Gerbe & Thouret, 2004). However, given the low vescicularity of the eruptive products and the large amount of degassing that happened from 1986, Gerbe & Thouret (2004) suggest this mechanism was not the main cause of the explosive activity. On the other hand, they proposed that the triggering factor could had been the occurrence of shallow tectonic earthquakes that might have increased the fracturing and consequently the infiltration of surface water from the ice cap melting. Another distinguishing feature is that the volumes of erupted magma were not enough to produce mudflows nor higher plumes which could possibly lead to pyroclastic density currents. However, activity, in terms of the frequency and intensity of the Vulcanian explosions, decreased gradually in the later years. In fact,

from 1997 Sabancaya volcano showed a very discontinuous and weak activity. The juvenile material erupted during this period was initially dacitic and then became more andesitic in composition, spanning a narrow range of compositions (60–64 wt. % of silica). The main magma body involved in the 1990–1998 eruption of Sabancaya consisted of dacitic magmas periodically recharged by more mafic magmas, leading to the formation and subsequent eruption of hybrid andesite; this hybrid origin was inferred from mineralogical and geochemical data (Gerbe & Thouret, 2004). Small explosions emitted gas and ash in 2000 and 2003, ash in 2000 and 2003, but the volcano then became quiet for a decade.

	1990-1992	1993-1994	1995-1997	Post 1997
Frequency of eruptions	every 20-30 minutes	Every 1-3 hours	5-6 events per day	< 5 events per day
Height of ash plumes	3 to 5 km high, rarely 7 km high	2-3 km high	1-3 km high	<1 km, 300-500 m high in average
Colour of plumes	light grey to grey	light-medium grey rarely white	light grey to white	mainly white
Dispersion of ash	about 10 km, rarely as much as 12 km		< 5 km	< 1 km
Percentage of juvenile fragments	10-15% in1990 to 40-50% in 1992	40-50 %	slight decrease	no juvenile tephra
Main eruptive activity	vulcanian and hydromagmatic		vulcanian, phreatomagmatic	phreatic or fumarolic

Fig. 2.1: Summary of the main characteristics of the 1990–1998 eruptions of Sabancaya (Gerbe & Thouret, 2004).

3.2. Recent activity (2016 – present-day)

The current eruptive cycle of Sabancaya began in November 2016 and is characterized by Vulcanian and phreatic explosions associated with constant water vapor, sulphur dioxide and ash emissions (MacQueen et al., 2020). After 15 years of quiescence and minor activity, degassing via fumaroles on the top of Sabancaya volcano resumed at the end of 2012 (Moussallam et al., 2017) and was followed by a strong increase in seismic activity from 2013 (Puma et al., 2016). Volcano-Tectonic (VT) seismic events are recognised to be possible precursors for an eruption, of any VEI and compositional range, at dormant volcanoes. These events can be triggered when magma injection into the chamber causes higher fluid

pressures, and a subsequent rapid increase of the injected magma can trigger an eruption (White & McCausland, 2016). High-momentum magnitude VT earthquakes ($M_W > 5$) occurred in 2013, but the related eruptive activity took up to 1 year from the first seismic event to manifest (two phreatic eruptions were recorded in 2014) (Jay et al., 2015).

In the meanwhile, degassing from the summit crater increased dramatically, both in terms of the density of emitted gases and in the height of the fumaroles (250 to 1500 m above the vent). In particular, sulphur dioxide emissions, that were essentially zero in 2012 increased to several 10s of metric tons per day (t/d) in 2013 and up to 100s t/d in 2014 (Kern et al., 2017).

At the beginning of 2016 extremely high emission rates of water vapor were measured at Sabancaya, consistent with the boiling-off of the hydrothermal system caused by the intrusion of magma to shallow depths. The detected water to sulphur dioxide molecular ratio was much higher than expected from the relative composition of these species in the magma (1000, about an order of magnitude larger than typically found in high-temperature volcanic gases), confirming the presence of a consistent amount of water circulating in the system (Kern et al., 2017). In the summer of 2016, new fumarolic areas were also noticed on the volcano flanks, with emissions appearing to increase in intensity over time (Global Volcanism Program, 2017).

In August 2016, an explosion followed by the emission of a gas and a minor ash plume, reaching 1 km above the vent, was the first sign of the imminent new eruptive phase of Sabancaya volcano. In fact, starting from 6 November 2016, a series of Vulcanian-style explosions and continuous low-level ash emissions began and, on 11 November 2016, Sabancaya experienced an explosive eruption producing a 3 km high plume with ash spreading and dispersion up to 50 km from the vent (Mariño et al., 2016). The main difference from the preceding activity was the change from a diffuse plume of mainly magmatic gases and water vapour to an ash-rich plume and, obviously, the occurrence of several explosions per day.

All the presented data were gathered by MacQueen et al. (2020) to propose a detailed model for magma-tectonic interaction during the 2012-2019 period. The leading result of the study is consistent with the hypothesis of fluid-overpressure-triggered seismicity, as hypothesised by Gerbe & Thouret (2004) and described above. This is a response of the propagation of fluid pressure due to a mafic intrusion at the main magma chamber level (almost 13 km depth below Hualca Hualca, inferred from interferometric data) feeding the Sabancaya plumbing system and then reactivating the shallow dacitic magma chamber (at almost 6 km depth, from petrologic data in Gerbe & Thouret (2004)). This is consistent with the increase in thermal anomaly and fumarolic activity that begun in 2012, but also with the petrologic evidence for magma mixing between dacite and a mafic intrusion in the 1990–1998 eruption, producing an andesitic magma. The similarity with the studies on the 1990-1998 eruption, can somehow find confirmation from the petrographic point of view: the eruptions products range from dacites to potassium-rich calc-alkaline andesites (60-65 wt. % of silica) (Manrique Llerena et al., 2018).

As previously stated, this eruptive period at Sabancaya volcano is still ongoing at the time of writing. However, differently from the 1990-1998 eruption, the activity has not been seen to decrease yet. In fact, during 14-20 June 2021, the Instituto Geofísico del Perú (IGP) reported a daily average of 80 explosions at Sabancaya, with gas-and-ash plumes reaching maximum heights of 2.3 km.

3.2.1. The July-August 2018 activity

This work will focus on Sabancaya eruptions that took place during July 2018 and August 2018. Based on data shared by the Volcano Observatories of the IGP and the Instituto Geológico, Minero y Metalurgico (InGeMMet), during this time the average daily number of explosions was 22 but ranged from 13 to 30, with maximum ash plume heights varying between 1.3 and 4.5 km above the crater. The drift directions were wind dependent. Sulphur dioxide emissions were variable and reached a maximum of 14859 tons per day. In particular, in the time span between 25 July and 14 August 2018 explosions averaged 20 per day, gas-and-ash plumes

rose as high as 3 km above the crater rim and spread up to 40 km towards the SE, E, and NE. Hybrid earthquakes were infrequent and of low magnitude. The sulphur dioxide gas flux peak was 5000 tons per day.

Fig 2.2: The beginning of the eruption at Sabancaya on 6 November 2016 (Bulletin of the Global Volcanism Network, vol. 42, no. 5).

4. Volcanic plumes

Volcanic plumes are mixtures of volcanic particles, gases, and entrained air that are produced by a variety of explosive eruptions. Bigger particles (> 2 millimetres) can be part of this mixture in the early development stages, while later only ash-sized particles are involved. The material is injected into the atmosphere, rises, and expands in a turbulent flow including multiple vortexes, and finally can be dispersed on a global scale. Buoyancy plays a fundamental role in the motion of plumes and determines how they interact with the atmosphere (Sigurdsson et al., 2015). Commonly, the generation of a Vulcanian plume, typical of Sabancaya activity, causes the fragmentation of the magma into small pieces and a mixture of solids, gases and, in some cases liquids, which are discharged from the vent. Rapid expansion of entrained air and of gases results in buoyancy generation and the rapid acceleration of the material into the atmosphere (Sigurdsson et al., 2015). Gases come out of solution in the magma – as magmas typically contain small amounts of dissolved volatile components such as water, carbon dioxide, and sulphur dioxide prior to eruption when they are stored beneath the Earth's surface – or are generated by heating of external water. In the case of Vulcanian style, cooling and crystallization of magma emplaced at shallow levels can lead to build-up of pressure from gas exsolution. If the conduit is blocked, catastrophic failure of the cap can lead to fragmentation and transient acceleration of a volume of magma out of the vent (Sigurdsson et al., 2015). Once a volcanic plume is ejected, the dominantly horizontal flow in the atmosphere begins to distort its structure and transport its material downwind. Initially, the changes caused by the plume-atmosphere interaction will be governed by the vertical and horizontal scales of the plume relative to atmospheric motions. In fact, the difference between relatively weak and strong plumes can be expressed in terms of the ratio of the horizontal wind speed to the upward plume speed. A weak plume, for which this ratio is large (>1), is greatly affected by the wind and maintain a cloudlike structure as they reach their maximum rise height. They take on a characteristic shape without a distinctive

umbrella region, and a vertical eruption column is unable to develop (Sigurdsson et al., 2015). The plume is not only bent over by the wind, but it also mixes with the turbulent atmosphere as it is carried along. This enhanced entrainment results in lower total plume heights for a given mass eruption rate as the wind speed increases because of the more rapid dilution of the plume's thermal energy by the entrained air (Sigurdsson et al., 2015). Sometimes, however, smaller plumes can have rather irregular outlines because of their susceptibility to local atmospheric motions (Sigurdsson et al., 2015).

Rise dynamics of volcanic plumes have been theoretically divided into two endmembers based on the ratio between the eruption duration (timescale for gas and ash injection in the atmosphere), and the rise and development time of the plume (Wilson et al., 1978; Chojnicki et al., 2015; Tournigand et al., 2017) (Fig 3.1). When the injection of volcanic material in the atmosphere lasts longer than the time required for the plume's height and shape to fully develop, the plume is referred to as sustained or in steady-state. Steady-state plume dynamics are characterized by a constant-rate source (Morton et al., 1956), and are usually associated with large volcanic plumes released by Plinian eruptions. On the other hand, plumes formed by a quasi-instantaneous release of ash and gas, that need relatively more time for the full rise and development of the plume, are often termed thermals or puffs (Turner, 1969). However, if the timescale of ash and gas release is similar to that of plume development and rise, the plume is described as intermediate between these two endmembers and is generally called a transient plume. Commonly, this type of plume well-describes Strombolian to Vulcanian activity, as they are related to unsteady discharge rates at the vent (Clarke et al., 2002). Usually, transient volcanic plume evolution can be subdivided into two main dynamical stages: at the beginning, the rise of the plume is dominated by the initial momentum associated with its ejection (gas-thrust phase); afterwards, the evolution of the plume is controlled by buoyancy originating from the entrainment and heating of the surrounding atmosphere (buoyancy-driven phase) (Patrick, 2007; Patrick et al., 2007).

During ascent, the volcanic plume changes its shape and width due to the entrainment of atmospheric air, with the plume developing through four main types, each of which have particular characteristics (Patrick, 2007; Fig. 3.2):

- Jets, that are high-velocity plume driven by high initial momentum
- Starting plumes, that are a buoyant plume where the circulating plume front emulates a thermal. This thermal at the plume front is continuously fed by the steady plume below it
- Rooted thermals, practically a starting plume whose thermal exhibits a strong vortex ring (an intermediate between the starting plume and the discrete thermal)
- Discrete thermals, consisting of detached fluid vortex powered solely by buoyancy

When motion is steady, plume spreading and entrainment can be related by the following expressions (Morton et al., 1956; Turner, 1962, 1979):

Steady jets: $\frac{dr}{dh} = 2\varepsilon$, (4.24)

Steady plumes: $\frac{dr}{dh} = \frac{6}{5}\varepsilon$, (4.25)

and

Discrete thermals: $\frac{dr}{dh} = \varepsilon$, (4.26)

where ε is the entrainment coefficient, r is the plume radius and h the height of the radius above the vent.

The shape evolution of volcanic plumes holds key information on eruptive processes occurring at the vent and has been investigated at several volcanoes (Tournigand et al., 2017). However, our understanding of the link between source conditions at the vent and plume morphology and evolution is still far from complete. Previous field observations have parameterized several aspects of transient plumes, including fundamental parameters, such as the height and width of the column, but also parameters which are more complex to be evaluated, e.g., the plume rise velocity, exit velocity, volume, temperature, or air entrainment (Tournigand et al., 2017).
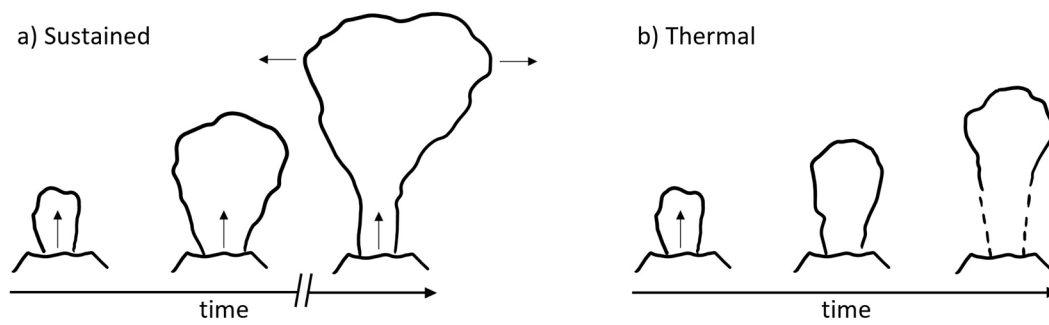
Fig. 3.1: Schematic sketch showing the time evolution of sustained- (a) and thermal-type (b) volcanic plumes. The timescales vary between the two types; note that for sustained plumes more time passes between the second and the third stage than between the first and the second).
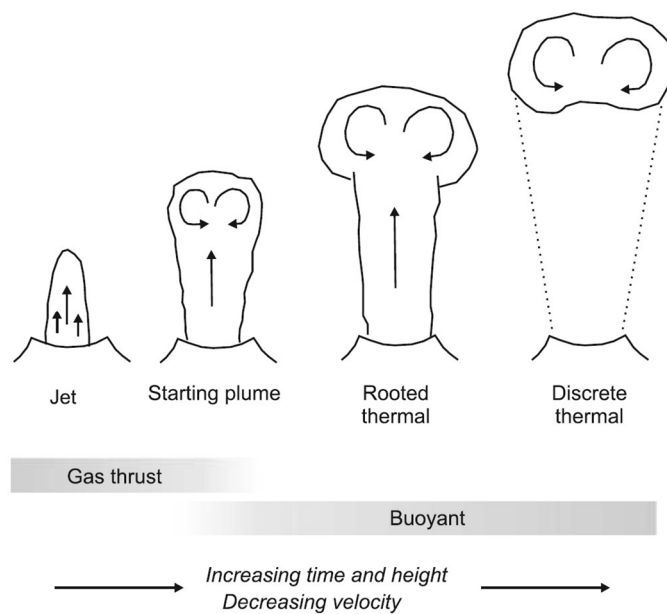

Fig. 3.2: Plume forms resulting from discrete explosions and their progression (Patrick, 2007).

5. Methodology

In the analysed timespan (July – August 2018), Vulcanian explosions at Sabancaya are short-lived events lasting a few tens of seconds up to a minute and consist of a release of ash and gas into a volcanic plume. The following methodology describes a multidisciplinary approach dedicated to analysing these explosions and improving the understanding of eruption plumes by extracting quantitative information from high-resolution videos. Analysis of volcanic plumes is an essential tool for understanding their dynamics and related hazards. Overall, relatively few eruption plumes have been recorded with visible wavelength videos with the original intention of making scientific measurements (Sparks, 1997).

The presented approach is pioneering because it is based on quasi-automatic MATLAB processing and analysis of frames extracted from high-resolution videos recorded in the field of visible light, with the aim of extracting geometric parameters of the volcanic plumes. A scrupulous literature search found two previous studies that pursued the same goal which are the software designed by Valade et al. (2014) (Plume Ascent Tracker) and the algorithm developed by Bombrun et al. (2018). The main difference between these studies and the algorithm proposed in this work is that the routines of both Valade et al. (2014) and Bombrun et al. (2018) are optimized for the analysis of thermal-wavelength videos. Both are open-source MATLAB-based algorithms, but Plume Ascent Tracker uses Graphical User Interfaces (GUIs), resulting in a more user-friendly environment for setting the video analysis parameters and choosing the outputs, while the algorithm of Bombrun et al. is fully-automated. However, the use of these two methods for analysing videos in the visible range of wavelengths presents some issues. On one hand, Plume Ascent Tracker lacks in the image analysis techniques; on the other hand, Bombrun et al.'s does not allow the binarization parameters to be varied, inhibiting optimal isolation of the plume. It is important to note that in the past these types of analysis were performed manually (e.g., Formenti et al., 2003), thus taking a long time for the user.

The main advantages of using videos recorded in the visible wavelengths are in terms of costs and resolution, as thermal (or, more generally, infrared) cameras are more expensive than normal cameras, and usually have lower resolutions. However, visible image analysis of volcanic plumes has almost always been overlooked, because of the difficulty in cleanly tracking the plume, especially in adverse meteorological conditions.

The following is a description of the steps that have been made to perform the analysis of the high-resolution videos recorded at Sabancaya. This algorithm has not been still validated for the analysis of thermal videos, but it can potentially work as equally well as for high-resolution visible videos, as thermal imagery works in grayscale (or false colours) and it should therefore be easier to isolate the plume-containing pixels from the others.

5.1. Video recordings

Video recordings were taken in the period between 28th July 2018 and 11th August 2018, with a mobile ground-based camera. The camera used for the recordings is a Canon Legria HFG40 with a frame rate of 50 fps and a resolution of 1920x1080
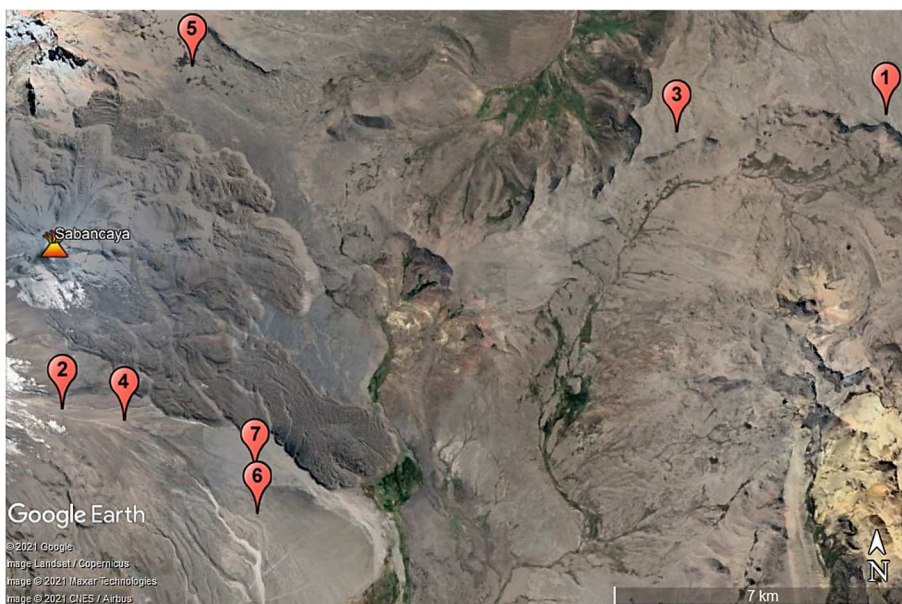

Fig. 4.1: Map of the area of Sabancaya showing the locations from where videos were recorded (Google Earth).

px^2. The location from where the plume is recorded was changed frequently and recorded into Global Positioning System (GPS) coordinates. Depending on the distance of the camera from the vent, the level of optical zoom was varied as well. During the campaign, the camera was continuously recording when in place, to avoid missing the start of the eruption. The field of view (FOV) of the camera is the angular extent of the image that is represented and depends on the focal length of the used lens and the size of the sensor in the camera. Unfortunately, the camera used in the field had a variable focal length, and it is impossible to know exactly what value the focal length was in each video. Thus, it was impossible to know a priori the horizontal and vertical FOVs, later needed to convert pixel positions into locations, through the manufacturing specifications.

5.2. Video analysis & calibration

The primary goal was to develop a new algorithm capable of detecting a moving plume and recording its dynamics through time. Two similar algorithms were perfected, one to semi-automize the process and another with a more user-friendly purpose. When run, both ask through a graphic interface what processing steps the user wants to perform, including frame extraction, image analysis and calibrations, and extraction of parameters (all combinations are possible). Thus, for example, once the frames are saved, it is not necessary to repeat the process of extraction of frames in case of the user wishes to re-run other parts of the algorithm. A critical part of the image processing is to automatically identify pixels of the image corresponding to the plume, and pixels corresponding to the sky, the background and the landscape. Typically, this is done by using thresholding and thus relies upon a strong difference in pixel intensity between the plume and its surroundings (Bombrun et al., 2018). The speed for the whole below explained video analysis is almost 0.08 frames/s (laptop specifications: Microsoft Corporation Surface Pro 4, Intel$^®$ Core™ m3-6Y30 CPU @ 0.90 GHz (4 CPUs), 1.5 GHz, 4 GB of RAM).

5.2.1. Extraction of frames

The first required step consists of temporally-cropping full-length videos so to analyse only the frames during which eruptions occurred; for Sabancaya, 49 videos of eruptions were selected from the full-length recordings (Table 1). An algorithm was then created using MATLAB 2018b to enable analysis of multiple videos and to save a resampled video with a frame rate of 1 frame per second. Thus, in this case one frame in every 50 was sampled. Computationally, the speed of frame extraction and saving is about 1.4 frames/s.

5.2.2. Image analysis techniques

As opposed to thermal images, images in the visible wavelengths are not in greyscale but composed of three channels (red, green, blue) and the contrast between the plume and the rest of the image is highly dependent on the meteorological conditions. Thus, an effectively segmented output requires a more elaborated strategy than for thermal imagery.

Multiple image analysis methods for detecting plume-containing pixels were first explored using ImageJ (Schneider et al., 2012) and, when a reliable strategy was found, this was then applied to all frames of the videos in MATLAB. The algorithm consists of the following procedure:

1. Before starting the processing, a graphical interface asks for user to input the threshold luminance value, used to create a binary image, and the neighbourhood size used for a median filter to be used later. The threshold has to be specified as a numerical scalar or numerical array with values in the range between 0 and 1, although, generally, values ranging from 0 and 0.2 should be used. This value can also be differentiated according to the image to which it will be applied, thus using different values for the first image than for the other ones.

2. The image analysis procedure (that will be described in detail later) is applied to the last frame to show a preliminary result of the analysis.

32

Table 1. List of explosions recorded in the visible wavelengths, with date and time of explosion onset. GPS coordinates of the location from where explosions were recorded are listed here, as the labels related to Fig. 4.1.

Explosion	Date	UTC-5	UTC	Camera GPS coordinates		Label
P1	08 August 2018	11:26	16:26	15°45'20.3" S	71°39'57.2" W	1
P2	08 August 2018	11:57	16:57	15°45'20.3" S	71°39'57.2" W	1
P3	09 August 2018	09:33	14:33	15°49'17.7" S	71°51'23.3" W	2a
P4	10 August 2018	13:51	18:51	15°49'17.7" S	71°51'23.3" W	2a
P5a	11 August 2018	12:46	17:46	15°45'34.2" S	71°42'53.8" W	3
P5b	11 August 2018	12:49	17:49	15°45'34.2" S	71°42'53.8" W	3
P6	29 July 2018	13:11	18:11	15°49'27.7" S	71°50'36.1" W	4a
P7	29 July 2018	14:04	19:04	15°49'27.7" S	71°50'36.1" W	4a
P8	30 July 2018	09:49	14:49	15°44'41.3" S	71°49'43.4" W	5
P9	30 July 2018	10:10	15:10	15°44'41.3" S	71°49'43.4" W	5
P10	30 July 2018	10:37	15:37	15°44'41.3" S	71°49'43.4" W	5
P11	30 July 2018	11:03	16:03	15°44'41.3" S	71°49'43.4" W	5
P12	30 July 2018	11:41	16:41	15°44'41.3" S	71°49'43.4" W	5
P13	30 July 2018	12:04	17:04	15°44'41.3" S	71°49'43.4" W	5
P14	31 July 2018	08:56	13:54	15°50'45.0" S	71°48'49.1" W	6
P15	31 July 2018	09:47	14:47	15°50'45.0" S	71°48'49.1" W	6
P16	31 July 2018	10:17	15:17	15°50'45.0" S	71°48'49.1" W	6
P17a	31 July 2018	10:42	15:42	15°50'45.0" S	71°48'49.1" W	6
P17b	31 July 2018	10:48	15:48	15°50'45.0" S	71°48'49.1" W	6
P18	31 July 2018	13:36	18:36	15°50'10.4" S	71°48'51.1" W	7
P19	31 July 2018	14:21	19:21	15°50'10.4" S	71°48'51.1" W	7
P20	01 August 2018	10:24	15:24	15°49'27.5" S	71°50'36.3" W	4b
P21	01 August 2018	10:41	15:41	15°49'27.5" S	71°50'36.3" W	4b
P22	01 August 2018	11:11	16:11	15°49'27.5" S	71°50'36.3" W	4b
P23	01 August 2018	12:04	17:04	15°49'27.5" S	71°50'36.3" W	4b
P24a	06 August 2018	10:12	15:12	15°49'17.1" S	71°51'23.3" W	2b
P24b	06 August 2018	10:25	15:25	15°49'17.1" S	71°51'23.3" W	2b
P25	06 August 2018	10:40	15:40	15°49'17.1" S	71°51'23.3" W	2b
P26	07 August 2018	10:47	15:47	15°49'17.7" S	71°51'23.2" W	2c
P27	07 August 2018	11:52	16:52	15°49'17.7" S	71°51'23.2" W	2c
P28	07 August 2018	12:50	17:50	15°49'17.7" S	71°51'23.2" W	2c
P29	07 August 2018	13:48	18:48	15°49'17.7" S	71°51'23.2" W	2c
P30	08 August 2018	10:00	15:00	15°45'20.3" S	71°39'57.2" W	1
P31	08 August 2018	13:54	18:54	15°45'20.3" S	71°39'57.2" W	1
P32	08 August 2018	14:08	19:08	15°45'20.3" S	71°39'57.2" W	1
P33a	08 August 2018	14:17	19:17	15°45'20.3" S	71°39'57.2" W	1
P33b	08 August 2018	14:50	19:50	15°45'20.3" S	71°39'57.2" W	1
P34	09 August 2018	09:20	14:20	15°49'17.7" S	71°51'23.3" W	2a
P35	10 August 2018	12:32	17:32	15°49'17.7" S	71°51'23.3" W	2a
P36	10 August 2018	12:42	17:42	15°49'17.7" S	71°51'23.3" W	2a
P37	29 July 2018	11:05	16:05	15°49'27.7" S	71°50'36.3" W	4a
P38	06 August 2018	14:20	19:20	15°49'17.1" S	71°51'23.3" W	2b
P39	08 August 2018	10:26	15:26	15°45'20.3" S	71°39'57.2" W	1
P40	08 August 2018	13:10	18:10	15°45'20.3" S	71°39'57.2" W	1
P41	08 August 2018	13:32	18:32	15°45'20.3" S	71°39'57.2" W	1
P42	10 August 2018	12:14	17:14	15°49'17.7" S	71°51'23.3" W	2a
P43	10 August 2018	12:42	17:42	15°49'17.7" S	71°51'23.3" W	2a
P44	10 August 2018	12:58	17:58	15°49'17.7" S	71°51'23.3" W	2a
P45	10 August 2018	13:30	18:30	15°49'17.7" S	71°51'23.3" W	2a

3. The algorithm recognizes the plume shape in the last frame by keeping only the biggest object that has value equal to 1 in the binary image.

4. A rectangular Region Of Interest (ROI) is drawn automatically around the plume to create a mask containing the supposed plume spreading area. If the ROI does not correspond to or incorporate well the plume (e.g., because of clouds are recognized as the bigger object), it can be drawn manually (zooming in is highly recommended).

5. As this part is inside a while loop, it can be run until a satisfactory output result – mainly in terms of segmentation – is obtained.

6. Once the plume seems to be well-isolated from the background in the last frame, the plume tracking algorithm can be applied to all frames through the image analysis procedure.

After these initial steps, the image analysis techniques (Fig. 4.2) can be applied to all frames (the speed for the image processing alone is about 0.39 frames/s):

1. To produce a segmented plume image for a given frame, other than the initial frame, three images are required (Fig. 4.2a):

   a. the image of the current frame;

   b. the image corresponding to the initial time, that is intended to be a reference for the background subtraction, i.e., the frame just prior to eruption initiation;

   c. the image of the previous frame.

2. The multichannel images (RGB) are split into their red, green and blue individual channels, obtaining images in which each pixel has a specific value of intensity.

3. Then, for each image, the red channel is subtracted from the blue channel, as this commonly increases the contrast between the plume and the background compared to other possible operations. The result is an image where the plume and the landscape are highlighted with respect of the rest of the image (Fig. 4.2b).

4. At this point, the segmentation process is applied by using the early defined threshold luminance value (Fig. 4.2c).

5. Next, in parallel, two partial masks are created by exploiting the difference in intensity of the images (Fig. 4.2d):

    a. The first one consists of the modulus of the subtraction of the segmented first frame from the segmented current frame, resulting in a binary image that shows the plume without the landscape, eventually the clouds (if they moved), and some noise;

    b. The second results from the modulus of the difference between the segmented current frame and the segmented previous frame, thus it consists of the local movement of the plume (and the clouds) after a time step and is fundamental to create a mask that fits the original plume extension (Fig. 4.3).

6. Combining these pipelines by summing the two produced masks (Fig. 4.2e) goes a long way towards enabling identification of the presence and evolution of the plume, but it is still not fully-isolated from the rest of the image.

7. The following step is a simple cleaning of the noise through a two-dimensional median filter, where each output pixel contains the median value in the earlier-defined neighbourhood area (a 4 by 4 area was always used) around the corresponding pixel in the input image (Fig. 4.2f).

8. A mask is then applied such that all the pixels outside the ROI are set equal to zero. This step is essential for ensuring that the plume is selected rather than other similar objects (e.g., atmospheric clouds, degassing clouds or the landscape if its intensity and contrast are similar to those of the plume) (Fig. 4.2g).

9. Next, only the largest object is kept, thus removing noise and objects not connected with the plume (Fig. 4.2h).

10. The last step is to fill the holes in the input binary image and the final image with the plume shape reconstruction is obtained (Fig. 4.2i).
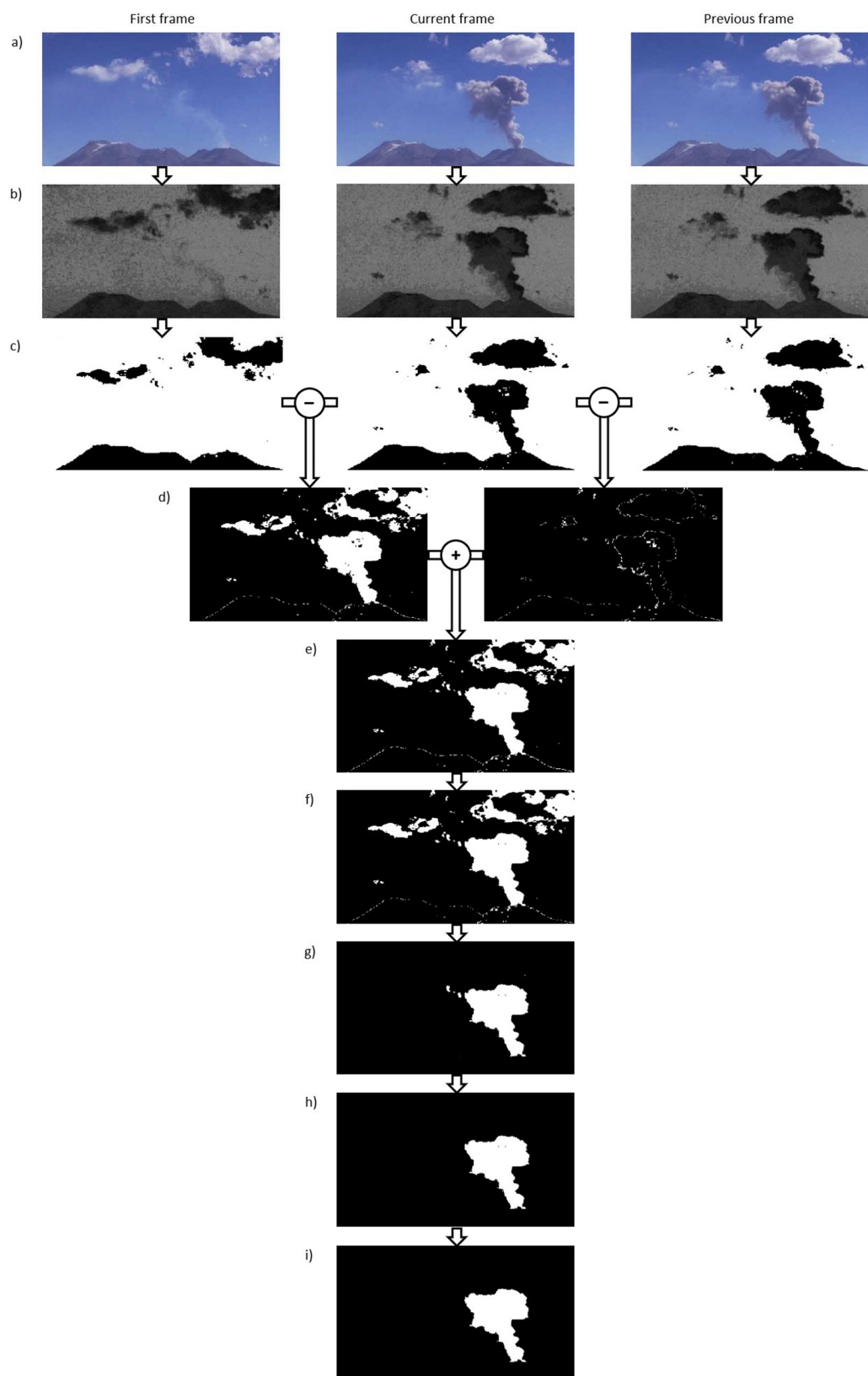
Fig. 4.2: Flow diagram of the plume tracking algorithm of a video recorded at Sabancaya (8th Aug 2018): a) original images, b) blue-red subtraction, c) segmentation, d) subtractions, e) sum of masks, f) median filter, g) ROI selection, h) biggest object and i) fill holes.

5.2.3. Geometric calibration

The subsequent step consists of a geometric calibration to convert pixel locations into physical coordinates (from pixel-units to metric-units). Here a method based on Bombrun et al. (2018) is followed. The vertical position z_i of a single pixel within the image is related to the distance of the camera from the plume Y and to geometric parameters of the camera (Fig. 4.4) through

$$z_i = \frac{Y}{2}\left(\tan\left(\phi - \frac{\beta_v}{2} + (i-1)\frac{\beta_v}{N_v}\right) + \tan\left(\phi - \frac{\beta_v}{2} + i\frac{\beta_v}{N_v}\right)\right), \tag{4.1}$$

where ϕ is the camera inclination with respect to the horizontal, β_v the vertical field of view (FOV), i the horizontal position (measured in pixels from the bottom of the image) of the pixel whose height is being measured and N_v the number of pixels in the vertical direction. Thus, β_v/N_v is the vertical angle subtended by a single pixel. Furthermore, the error estimation on the pixel position is

$$\Delta z_i = \frac{Y}{2}\left(\tan\left(\phi - \frac{\beta_v}{2} + i\frac{\beta_v}{N_v}\right) - \tan\left(\phi - \frac{\beta_v}{2} + (i-1)\frac{\beta_v}{N_v}\right)\right). \tag{4.2}$$

Thus, the farther from the centre of the image a pixel, the more the pixel's vertical extent increases. On the other hand, the horizontal pixel extent x_i is approximately constant across the image and can be defined as

$$x_i = 2Y\,tan\left(\frac{\beta_h}{2}\right), \tag{4.3}$$

where β_h is the horizontal FOV. In these equations, the distance of the camera from the plume Y is calculated both from the camera to the nearest side of the crater and from the camera to the to the farthest side of the crater, as the exact positioning of the vent is unknown. These equations are applied by the algorithm to get the real extent of a pixel and of an image.

The horizontal FOV was determined by comparing the panorama of the video with a panorama taken at the camera GPS location from the ground-level viewer in Google Earth (Fig. 4.5). Then two lines were traced, using the measure tool, from the camera site to one of the projected limits of the image extent each, approximating it as well as possible (Fig. 4.6). While drawing these lines, their orientations was annotated to determine the horizontal FOV by a simple

subtraction. Subsequently, the vertical FOV was calculated by simply applying the proportion

$$\beta_h : \beta_v = N_h : N_v \, , \tag{4.4}$$

where N_h is the number of pixels in the horizontal direction. Once the horizontal FOV is known, it is possible to measure the horizontal distance between the camera position and the vent with the measure tool and along the direction of camera orientation (Fig. 4.6). These operations were performed for each different recording condition.

5.2.4. *Correction for wind direction*

The following part of the algorithm, regarding the correction of the pixel's location for the wind direction, follows a newly-developed and innovative procedure described in Snee et al. (in prep).

It has already been noted that wind can cause a volcanic plume to be bent-over (thus behaves as weak), and transport the material downwind. Therefore, it is necessary to apply a correction that accounts for the local wind field to obtain the real geometrical parameters of the plume.

To apply the wind correction the fundamental parameter needed is the wind direction. This information can be extracted from local weather stations or through numerical weather predictions. Since there are no weather stations recording wind conditions in the proximity of Sabancaya volcano, the ERA5 hourly data on pressure levels were downloaded. ERA5 is the fifth generation European Centre for Medium-Range Weather Forecast (ECMWF) reanalysis for global climate and weather. Reanalysis combines model data with observations from across the world into a globally complete and consistent dataset using the laws of physics (Hersbach et al., 2018). Data assimilation is based on the method used by numerical weather prediction centres but applied to the past. In this way, a previous forecast is combined with available observations in an optimal way to produce a best estimate of the state of the atmosphere, called reanalysis. ERA5 data are gridded to a regular
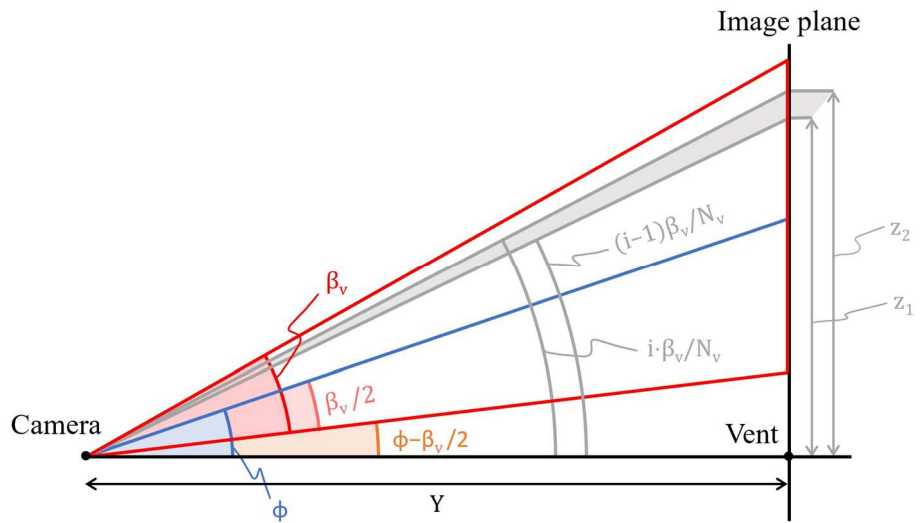
Fig. 4.4: Sketch showing the geometrical calibration. Red lines are the image limits, the blue one the line to the centre of the image and the grey ones represent the extent of a single pixel (exaggerated). Figure modified from Bombrun et al. (2018).
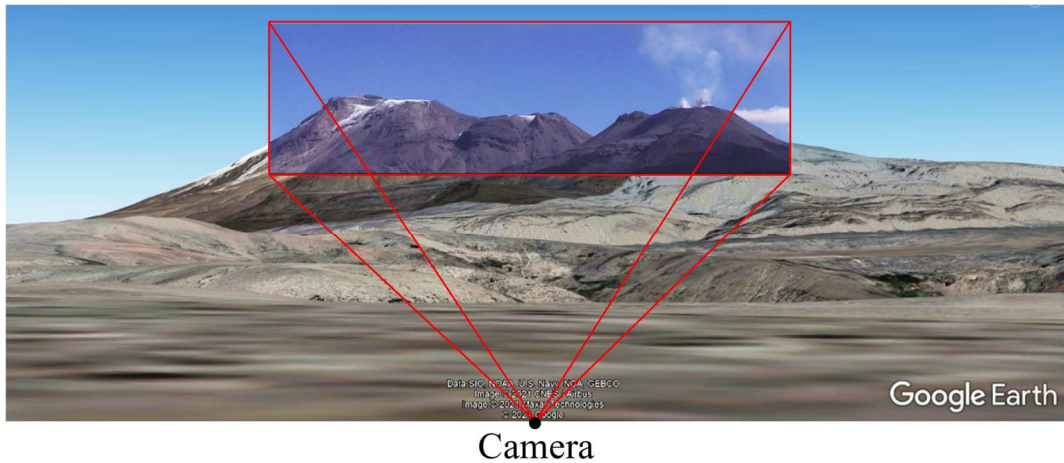

Fig. 4.5: Example of a ground-level view in Google Earth from a camera recording site (n°3) with the recorded image extent superimposed to show how the horizontal FOV was defined.
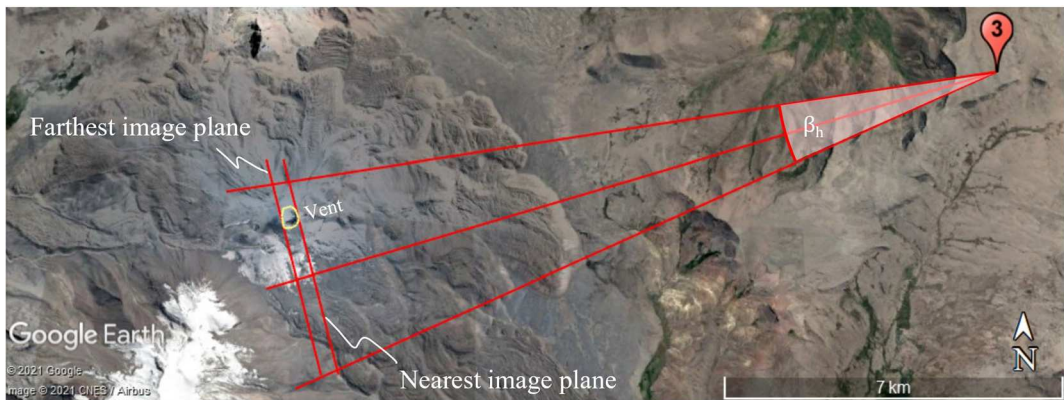

Fig. 4.6: Geometric construction to determine the horizontal FOV and the distance of the camera from the vent in the two possible planes (Google Earth).

latitude-longitude grid of 0.25° and have vertical resolution distributed into 37 pressure levels that cover a range from 1000 hPa to 1 hPa. Data downloaded from this platform are given to the user in NetCDF file format, easily readable into MATLAB. The 37 pressure levels can be related to a specified height by downloading and then dividing the geopotential (the gravitational potential energy of a unit mass, at a particular location, relative to mean sea level, measured in m^2/s^2) by the acceleration of gravity (9.81 m/s^2). The other parameters to be downloaded from the dataset are the U-component of wind velocity and the V-component of wind velocity, respectively the eastward and northward components of the wind velocity (a negative sign indicates the opposite cartesian direction). By using the magnitude and direction of these two parameters, it is easy to obtain the wind direction with the trigonometric relations (Fig. 4.7)

$$\theta = \tan^{-1}\left(\frac{V}{U}\right),$$ (4.5)

and

$$\omega = \begin{cases} 90° - \theta, & U \geq 0 \wedge V \geq 0 \\ 90° + \theta, & U \geq 0 \wedge V \leq 0 \\ 270° - \theta, & U \leq 0 \wedge V \leq 0 \\ 270° + \theta, & U \leq 0 \wedge V \geq 0 \end{cases},$$ (4.6)

where θ is the angle between the E-W axis and the wind velocity vector, U and V the U- and V-components of wind velocity, and ω the wind direction measured relative to N.

Through this, different wind directions referring to different height levels are obtained. However, it is important to use the height levels that are at a lower or similar height of the plume. This is done through a preliminary analysis of the plume height (see section 4.3.1). If the obtained values are similar, an average of them can be used for the analysis.

To apply the correction for wind direction, the location of a hypothetical plume pixel in the image plane $P_i(x_i, y_i, z_i)$ is firstly assumed (for z_i see Eq. 4.1)

$$x_i = Y\left(\tan\left(\frac{\beta_h}{2} - \frac{n_v \beta_h}{N_h}\right) + \tan\left(\frac{i\beta_h}{N_h} - \frac{\beta_h}{2}\right)\right)$$ (4.7)
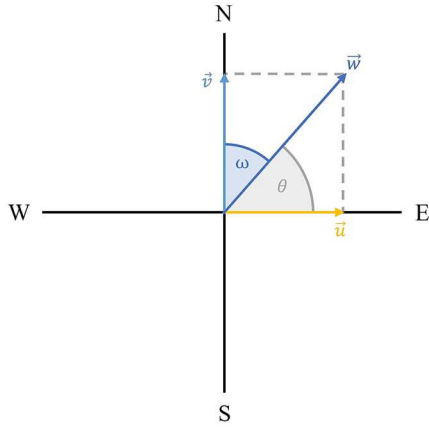
$$y_i = 0$$ (4.8)

Fig. 4.7: Representation of the wind velocity and its components in a cardinal directions system. The wind direction can be derived by simply applying Eqs. 4.5-4.6.

where all the parameters are already defined apart from n_v, which is the horizontal pixel containing the vent position, as measured from the left-hand side. Notice that Eq. 4.7 now replaces Eq. 4.3. The y_i coordinate is zero because it is considered to be at the vent level, so lying on the image plane (Fig. 4.8).

Once defined the pixel in the image plane, its coordinates should be trasformed to those in the wind-corrected plane $P_w(x_w, y_w, z_w)$:

$$x_w = x_i \left(1 \pm \frac{\sin\chi \sin\left(\frac{i\beta_h}{N_h} - \frac{\beta_h}{2}\right)}{\cos\left(\pm\chi - \frac{i\beta_h}{N_h} + \frac{\beta_h}{2}\right)} \right), \tag{4.9}$$

$$y_w = y_i \pm \frac{x_i \sin\chi \cos\left(\frac{i\beta_h}{N_h} - \frac{\beta_h}{2}\right)}{\cos\left(\pm\chi - \frac{i\beta_h}{N_h} + \frac{\beta_h}{2}\right)}, \tag{4.10}$$

$$z_w = z_i \pm y_w \tan\left(\phi - \frac{\beta_v}{2} + \frac{j\beta_v}{N_v}\right), \tag{4.11}$$

where χ is the angle between the image plane and the wind-corrected plane and j the vertical position (from the bottom of the image) of the pixel whose height is being measured.

As can be seen, terms in these equations can be positive or negative depending on the geometrical constraints of the different conditions (Fig. 4.9). Thus, their demonstration is shown in Figs. 4.9 and 4.10 and can be summarized as follows. Considering the camera orientation and the image plane respectively as the y and x axis of a Cartesian plane:

1. If the wind direction is towards the II or IV quadrant, and:

   i. The pixel position P_i in the image plane is to the right of the vent:

$$x_w = x_i \left(1 + \frac{\sin\chi \sin\left(\frac{i\beta_h}{N_h} - \frac{\beta_h}{2}\right)}{\cos\left(-\chi - \frac{i\beta_h}{N_h} + \frac{\beta_h}{2}\right)} \right) \tag{4.12}$$

$$y_w = y_i - \frac{x_i \sin\chi \cos\left(\frac{i\beta_h}{N_h} - \frac{\beta_h}{2}\right)}{\cos\left(-\chi - \frac{i\beta_h}{N_h} + \frac{\beta_h}{2}\right)} \tag{4.13}$$

   ii. The pixel position P_i in the image plane is to the left of the vent:

$$x_w = x_i \left(1 - \frac{\sin\chi \sin\left(\frac{i\beta_h}{N_h} - \frac{\beta_h}{2}\right)}{\cos\left(-\chi - \frac{i\beta_h}{N_h} + \frac{\beta_h}{2}\right)} \right) \tag{4.14}$$

$$y_w = y_i + \frac{x_i \sin\chi \cos\left(\frac{i\beta_h}{N_h} - \frac{\beta_h}{2}\right)}{\cos\left(-\chi - \frac{i\beta_h}{N_h} + \frac{\beta_h}{2}\right)} \tag{4.15}$$

2. If the wind direction is towards the I or III quadrant, and:

   i. The pixel position P_i in the image plane is to the right of the vent:

$$x_w = x_i \left(1 - \frac{\sin\chi \sin\left(\frac{i\beta_h}{N_h} - \frac{\beta_h}{2}\right)}{\cos\left(\chi - \frac{i\beta_h}{N_h} + \frac{\beta_h}{2}\right)} \right) \tag{4.16}$$

$$y_w = y_i + \frac{x_i \sin\chi \cos\left(\frac{i\beta_h}{N_h} - \frac{\beta_h}{2}\right)}{\cos\left(\chi - \frac{i\beta_h}{N_h} + \frac{\beta_h}{2}\right)} \tag{4.17}$$

   ii. The pixel position P_i in the image plane is to the left of the vent:

$$x_w = x_i \left(1 + \frac{\sin\chi \sin\left(\frac{i\beta_h}{N_h} - \frac{\beta_h}{2}\right)}{\cos\left(\chi - \frac{i\beta_h}{N_h} + \frac{\beta_h}{2}\right)} \right) \tag{4.18}$$

$$y_w = y_i - \frac{x_i \sin\chi \cos\left(\frac{i\beta_h}{N_h} - \frac{\beta_h}{2}\right)}{\cos\left(\chi - \frac{i\beta_h}{N_h} + \frac{\beta_h}{2}\right)} \tag{4.19}$$
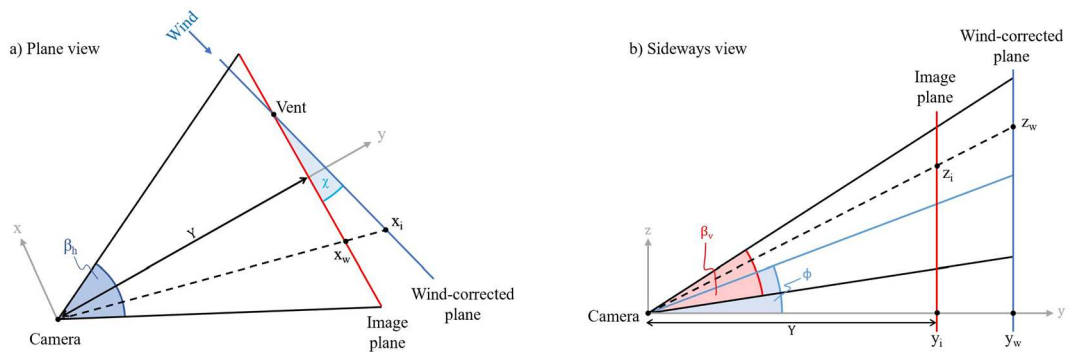
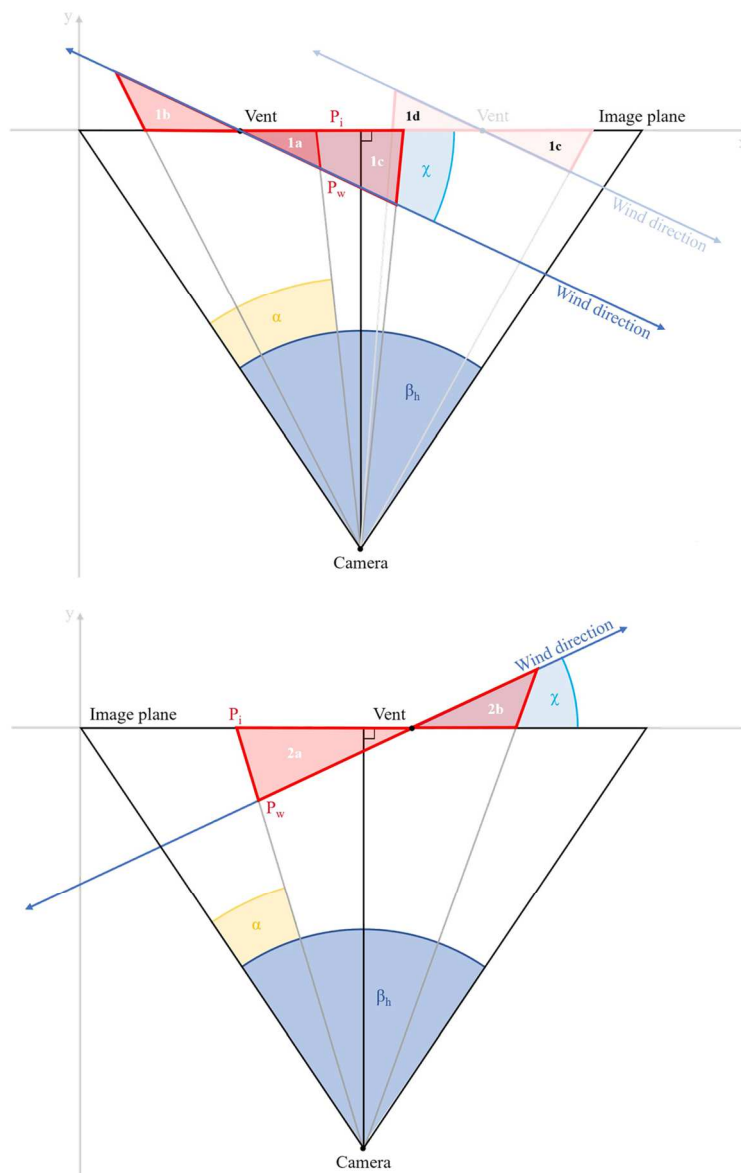**Fig. 4.8**: Sketch showing the P_i and P_w coordinates.

Fig. 4.9: Sketches showing two distinguished different cases, used to define the equation to then apply the wind correction.

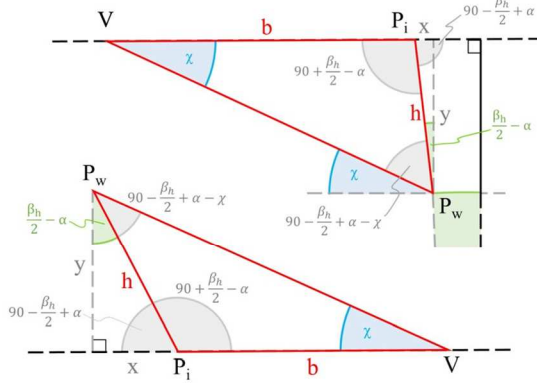**Case 1**. Wind blowing towards the II or IV quadrant of an imaginary stereonet centred into the vent.

a. Pixels are to the right of the vent.

$$\frac{h}{\sin\chi} = \frac{b}{\sin\left(90-\frac{\beta_h}{2}+\alpha-\chi\right)} \quad, \quad where \ \alpha = i\frac{\beta_h}{N_h} \ \Rightarrow \ h = \frac{b\sin\chi}{\sin(90)\cos\left(-\frac{\beta_h}{2}+\alpha-\chi\right)+\cos(90)\sin\left(-\frac{\beta_h}{2}+\alpha-\chi\right)} = \frac{b\sin\chi}{\cos\left(\alpha-\frac{\beta_h}{2}-\chi\right)}$$

$$x = h\sin\left(\frac{\beta_h}{2}-\alpha\right) \quad \& \quad y = h\cos\left(\frac{\beta_h}{2}-\alpha\right)$$

$$P_w(x) = P_i(x) + h\sin\left(\frac{\beta_h}{2}-\alpha\right)$$

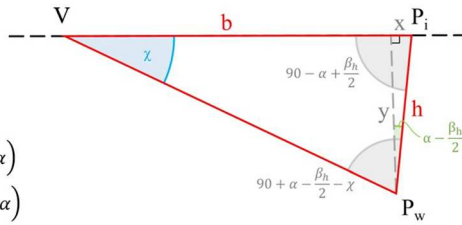$$P_w(y) = P_i(y) - h\cos\left(\frac{\beta_h}{2}-\alpha\right)$$

b. Pixels are to the left of the vent.

$$\frac{h}{\sin\chi} = \frac{b}{\sin\left(90-\frac{\beta_h}{2}+\alpha-\chi\right)} \ \Rightarrow \ h = \frac{b\sin\chi}{\cos\left(\alpha-\frac{\beta_h}{2}-\chi\right)}$$

$$x = h\sin\left(\frac{\beta_h}{2}-\alpha\right) \quad \& \quad y = h\cos\left(\frac{\beta_h}{2}-\alpha\right)$$

$$P_w(x) = P_i(x) - h\sin\left(\frac{\beta_h}{2}-\alpha\right)$$

$$P_w(y) = P_i(y) + h\cos\left(\frac{\beta_h}{2}-\alpha\right)$$

c. Pixels are to the right of the vent, but α > β/2.

$$\frac{h}{\sin\chi} = \frac{b}{\sin\left(90+\alpha-\frac{\beta_h}{2}-\chi\right)} \ \Rightarrow \ h = \frac{b\sin\chi}{\cos\left(\alpha-\frac{\beta_h}{2}-\chi\right)}$$

$$x = h\sin\left(\alpha-\frac{\beta_h}{2}\right) \quad \& \quad y = h\cos\left(\alpha-\frac{\beta_h}{2}\right)$$

$$P_w(x) = P_i(x) - h\sin\left(\alpha-\frac{\beta_h}{2}\right) = P_i(x) + h\sin\left(\frac{\beta_h}{2}-\alpha\right)$$

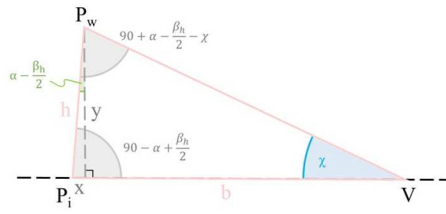$$P_w(y) = P_i(y) - h\cos\left(\alpha-\frac{\beta_h}{2}\right) = P_i(y) - h\cos\left(\frac{\beta_h}{2}-\alpha\right)$$

d. Pixels are to the left of the vent, but α > β/2.

$$\frac{h}{\sin\chi} = \frac{b}{\sin\left(90+\alpha-\frac{\beta_h}{2}-\chi\right)} \ \Rightarrow \ h = \frac{b\sin\chi}{\cos\left(\alpha-\frac{\beta_h}{2}-\chi\right)}$$

$$x = h\sin\left(\alpha-\frac{\beta_h}{2}\right) \quad \& \quad y = h\cos\left(\alpha-\frac{\beta_h}{2}\right)$$

$$P_w(x) = P_i(x) + h\sin\left(\alpha-\frac{\beta_h}{2}\right) = P_i(x) - h\sin\left(\frac{\beta_h}{2}-\alpha\right)$$

$$P_w(y) = P_i(y) + h\cos\left(\alpha-\frac{\beta_h}{2}\right) = P_i(y) + h\cos\left(\frac{\beta_h}{2}-\alpha\right)$$

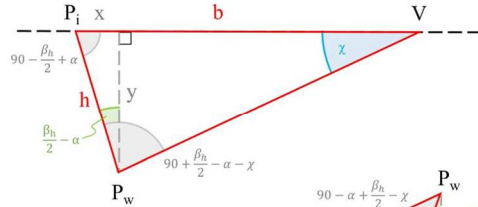**Case 2**. Wind blowing towards the I or III quadrant of an imaginary stereonet centred into the vent.

a. Pixels to the left of the vent.

$$\frac{h}{\sin\chi} = \frac{b}{\sin\left(90+\frac{\beta_h}{2}-\alpha-\chi\right)} \ \Rightarrow \ h = \frac{b\sin\chi}{\sin(90)\cos\left(\frac{\beta_h}{2}-\alpha-\chi\right)+\cos(90)\sin\left(\frac{\beta_h}{2}-\alpha-\chi\right)} = \frac{b\sin\chi}{\cos\left(\frac{\beta_h}{2}-\alpha-\chi\right)} = \frac{b\sin\chi}{\cos\left(\alpha-\frac{\beta_h}{2}+\chi\right)}$$

$$x = h\sin\left(\frac{\beta_h}{2}-\alpha\right) \quad \& \quad y = h\cos\left(\frac{\beta_h}{2}-\alpha\right)/$$

$$P_w(x) = P_i(x) + h\sin\left(\frac{\beta_h}{2}-\alpha\right)$$

$$P_w(y) = P_i(y) - h\cos\left(\frac{\beta_h}{2}-\alpha\right)$$

b. Pixels to the right of the vent.

$$\frac{h}{\sin\chi} = \frac{b}{\sin\left(90-\alpha+\frac{\beta_h}{2}-\chi\right)} \ \Rightarrow \ h = \frac{b\sin\chi}{\cos\left(\alpha-\frac{\beta_h}{2}+\chi\right)}$$

$$x = h\sin\left(\alpha-\frac{\beta_h}{2}\right) \quad \& \quad y = h\cos\left(\alpha-\frac{\beta_h}{2}\right)$$

$$P_w(x) = P_i(x) + h\sin\left(\alpha-\frac{\beta_h}{2}\right) = P_i(x) - h\sin\left(\frac{\beta_h}{2}-\alpha\right)$$

$$P_w(y) = P_i(y) + h\cos\left(\alpha-\frac{\beta_h}{2}\right) = P_i(y) + h\cos\left(\frac{\beta_h}{2}-\alpha\right)$$
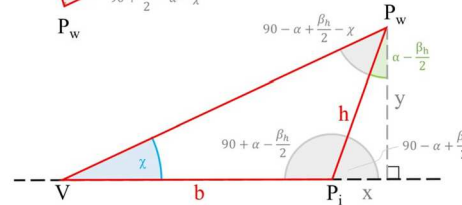
Fig. 4.10: Demonstration of Eqs. 4.12-4.19 (triangles correspond to those in Fig. 4.9). As in case 1c and 1d, vent and pixel position with respect to the observing point can vary, but do not affect the final formula (assumed also for case 2).

On the other hand, the change of sign in Eq. 4.11 is because of the motion of the plume affected by the wind. In fact, if the wind moves the plume away from the camera (e.g., Fig. 4.8) the shift, represented by the second part of the right-hand side of Eq. 4.11, must be positive. Otherwise, if the plume is moving towards the camera, it must be negative. Ultimately, this is the equation used to retrieve the height of each pixel.

The last parameter to be set is the angle between the image plane and the wind-corrected plane χ. Although this is intuitive from a theoretical point of view, it is tricky to define practically (more detailed demonstration in Figs. 4.11a-b). First of all, to obtain the simplest definition of χ, when the wind direction ω is greater than N180 it should be corrected as

$$\omega' = \begin{cases} \omega, & 0° \leq \omega < 180° \\ \omega - 180°, & 180° \leq \omega < 360° \end{cases}. \tag{4.20}$$

Then δ, an auxiliary angle that is needed to calculate χ, is defined as

$$\delta = \begin{cases} \Omega + 90°, & 0 \leq \Omega < 90° \\ \Omega - 90°, & 90° \leq \Omega < 270° \\ \Omega - 270°, & 270° \leq \Omega < 360° \end{cases}, \tag{4.21}$$

where Ω is the camera orientation (measured with respect to N). And finally, the angle between the image plane and the wind-corrected plane χ is

$$\chi = \begin{cases} |\delta - \omega'|, & |\delta - \omega'| < 90° \\ 180° - |\delta - \omega'|, & |\delta - \omega'| > 90° \end{cases}. \tag{4.22}$$

Once the geometric and wind correction are performed, it is possible to use the obtained true height (a N_h x N_v matrix) and width (a N_h x 1 vector) of the images to define the geometric parameters of the plume. The whole calibration process takes almost 17 s for a 1920x1080 image.

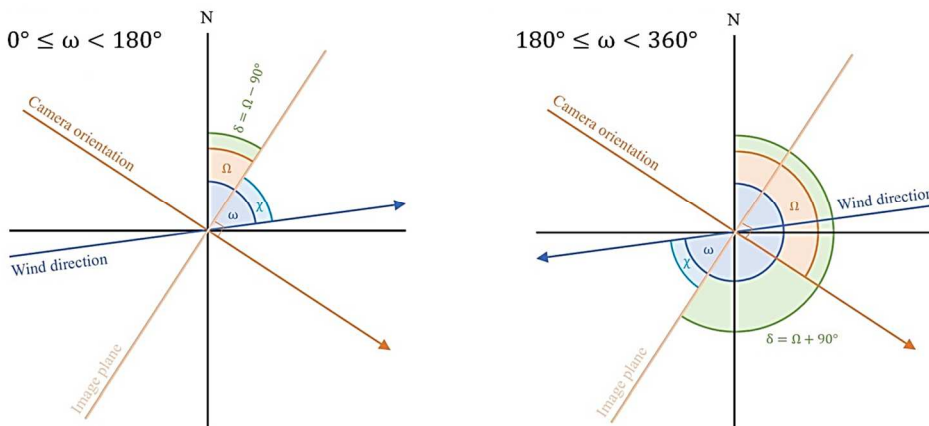For a camera orientation angle of $0° \leq \Omega < 90°$, for different wind direction angles:
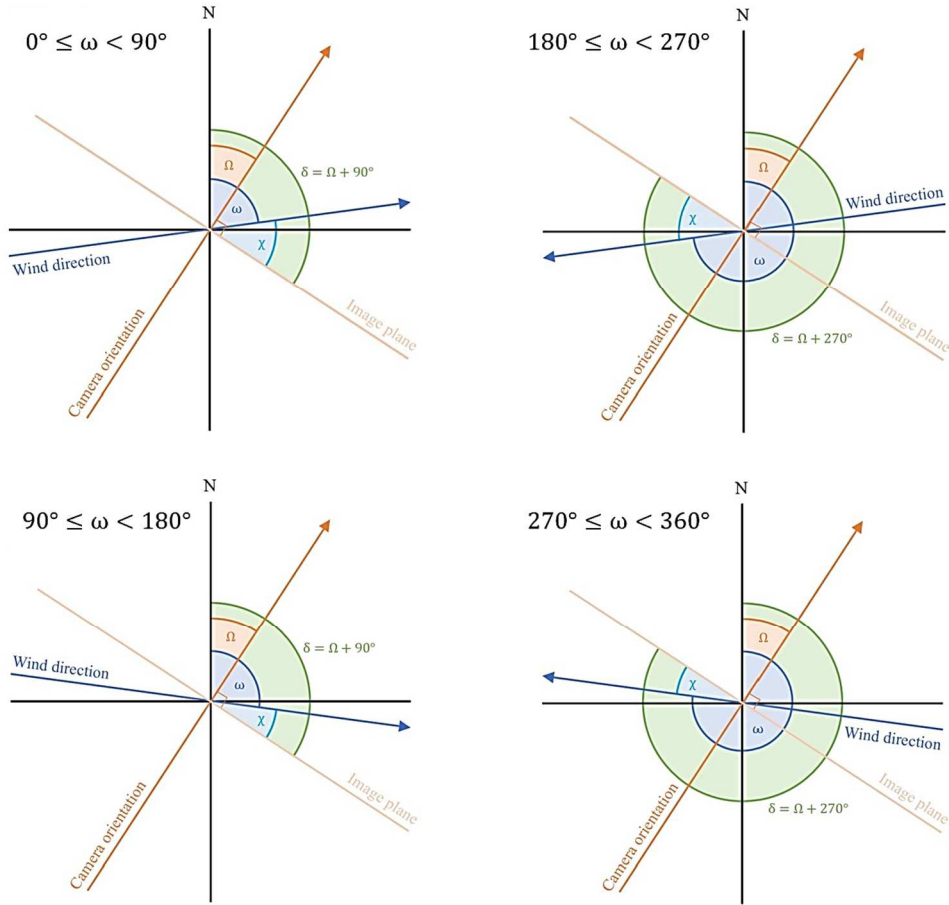
That can be simplified as:

$$\omega' = \begin{cases} \omega & 0° \leq \omega < 180° \\ \omega - 180° & 180° \leq \omega < 360° \end{cases} \quad \Rightarrow \quad \delta = \Omega + 90°, \ 0 \leq \Omega < 90° \quad \Rightarrow \quad \chi = \delta - \omega'$$

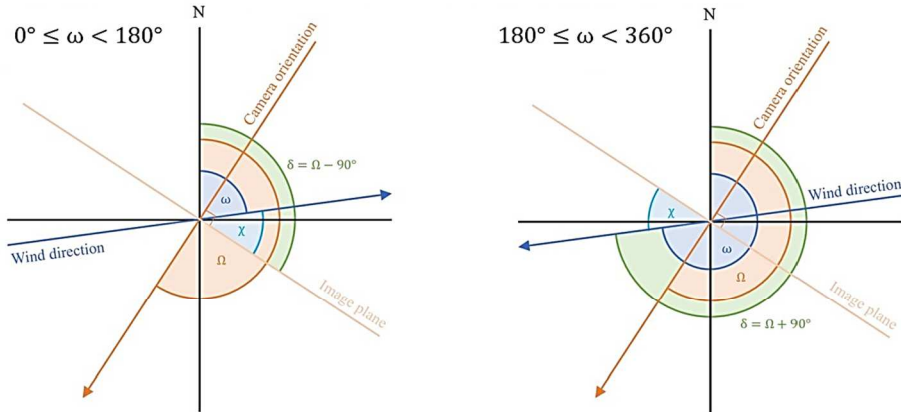Then, for a camera orientation angle of $90° \leq \Omega < 180°$ (considering a 180° step for wind direction):

Thus, in general, since in this case $\omega > \delta$:

$$\omega' = \begin{cases} \omega & 0° \leq \omega < 180° \\ \omega - 180° & 180° \leq \omega < 360° \end{cases} \quad \Rightarrow \quad \delta = \begin{cases} \Omega + 90° & 0 \leq \Omega < 90° \\ \Omega - 90° & 90° \leq \Omega < 180° \end{cases} \quad \Rightarrow \quad \chi = |\delta - \omega'|$$
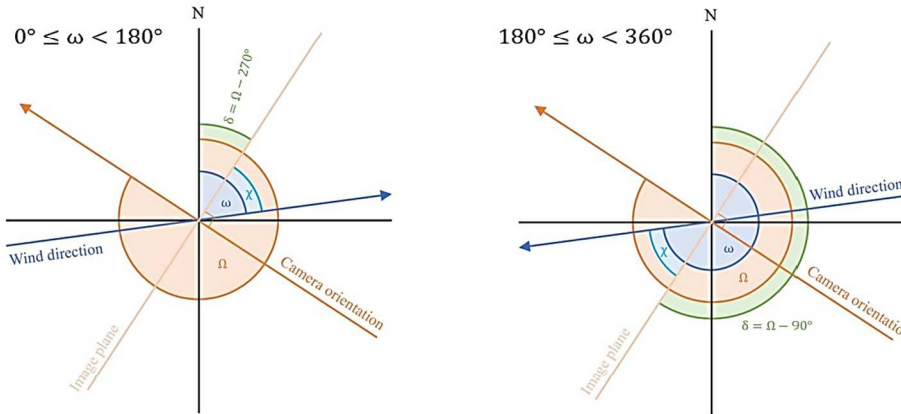
Fig. 4.11a: Demonstration of Eqs. 4.20-4.22.

Then, for a camera orientation angle of $180° \leq \Omega < 270°$ (considering a 180° step for wind direction):

Thus, in general:

$$\omega' = \begin{cases} \omega & 0° \leq \omega < 180° \\ \omega - 180° & 180° \leq \omega < 360° \end{cases} \Rightarrow \quad \delta = \begin{cases} \Omega + 90° & 0 \leq \Omega < 90° \\ \Omega - 90° & 90° \leq \Omega < 270° \end{cases} \Rightarrow \quad \chi = |\delta - \omega'|$$
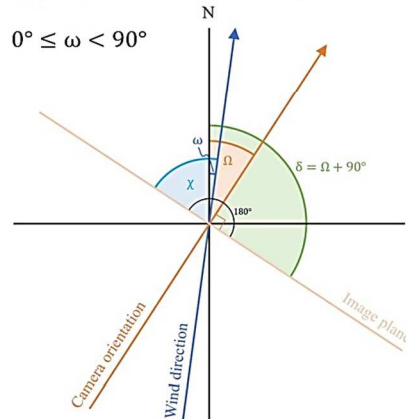
Again, for a camera orientation angle of $270° \leq \Omega < 360°$ (considering a 180° step for wind direction):

Thus, in general:

$$\omega' = \begin{cases} \omega & 0° \leq \omega < 180° \\ \omega - 180° & 180° \leq \omega < 360° \end{cases} \Rightarrow \quad \delta = \begin{cases} \Omega + 90° & 0° \leq \Omega < 90° \\ \Omega - 90° & 90° \leq \Omega < 270° \\ \Omega - 270° & 270° \leq \Omega < 360° \end{cases} \Rightarrow \quad \chi = |\delta - \omega'|$$

Then, in the $0° \leq \Omega < 90°$ case, if considering a wind direction closer to the camera orientation and the N:

This happens when the $|\delta - \omega|$ angle is obtuse, and we are looking for the acute one. Thus, reassuming:

$$\omega' = \begin{cases} \omega, & 0° \leq \omega < 180° \\ \omega - 180°, & 180° \leq \omega < 360° \end{cases}$$

$$\delta = \begin{cases} \Omega + 90°, & 0 \leq \Omega < 90° \\ \Omega - 90°, & 90° \leq \Omega < 270° \\ \Omega - 270°, & 270° \leq \Omega < 360° \end{cases}$$

$$\chi = \begin{cases} |\delta - \omega'|, & |\delta - \omega'| < 90° \\ 180° - |\delta - \omega'|, & |\delta - \omega'| > 90° \end{cases}$$

Fig. 4.11b: Demonstration of Eqs. 4.20-4.22.

5.3. Extraction of parameters

Image processing methods and calibration of the images to get quantitative physical values in metres are used to extract geometric parameters, and to provide information on turbulent structures within the plume. The first-order analysis consists of the calculating from the identified plume the main dimensions, i.e. height and width (as a function of height), as a function of time. A second-order analysis is then performed to retrieve the ascent velocity of the plume in the atmosphere and the entrainment coefficient. Automatic calculation of air entrainment is quite complicated and thus is not implemented in the MATLAB algorithm. The speed for determining the parameters (excluding air entrainment) is almost 0.1 frames/s, so it is very computationally expensive, mainly due to the calculation of the width in the wind-corrected plane. The determined values and relative errors deriving from the calibration processes are then automatically saved and plotted into an Excel file (Fig. 4.12): this procedure is not frame number-dependent, and requires almost 106.6 s.

5.3.1. Height

The plume height is defined as the uppermost pixel of the plume mask (Fig. 4.13a). The algorithm outputs both the height calculated in the image plane and that in the wind-corrected plane. This is useful to check if the wind correction is working as it supposed to do, but also to use these parameters in the case the wind is blowing in a direction parallel to the camera orientation (see also section 5.1).

In the case of plume height in the image plane, the algorithm is set to subtract the height of the vent (that corresponds to the height from the camera plane) from the calibrated highest value, to then obtain a relative height with respect to the vent. The resulting plume height is an average that accounts for the error related to the geometric calibration and for the distance of the camera from the vent.

On the other hand, the calculation of plume height in the wind-corrected plane is similar but requires a more complicated programming, in terms of finding the

maximum value. This happens because the wind-calibrated height of pixels is represented by a matrix (no more a vector, like in the previous case).

5.3.2. *Width*

The width of the plume is firstly calculated at each pixel level, then the maximum width is found to show the plume spreading upon its ascent (Fig 4.13a). Again, the width is calculated in the image plane and that in the wind-corrected plane as calculated by the algorithm.

In the first instance, calculation of width in the image plane is simply done by summing the values equal to 1 for each row and multiplying the obtained value by a scale factor that represents the extent of a pixel in the image (practically Eq. 4.3 divided by the total number of pixels in the horizontal direction, 1920). Then, the maximum value was selected for each frame to have a value evolving as a function of time.

The plume width in the wind-corrected plane is difficult to be calculated, even more so than height, and is susceptible to several inaccuracies. Since the plume is not in the image plane anymore, the plume contour points at the same height are linked by a line that is oblique with respect to the horizontal (Fig 4.13b). Thus, the width cannot be found by considering the rows of the plume mask, but is performed by comparing the height values on both sides of a calibrated plume mask, finding the most similar value between these two sides and, knowing their pixel calibrated location from Eq. 4.9 and 4.10, by calculating the Euclidean distance between them

$$w = \sqrt{(x_2 - x_1)^2 + (y_2 - y_1)^2} \, , \tag{4.23}$$

where w is the plume width at a specified height and time and x_1, x_2, y_1, y_2 are the coordinates of the two points at the contour of the plume. Once this has been done for each row, the maximum width of the plume can be easily calculated.
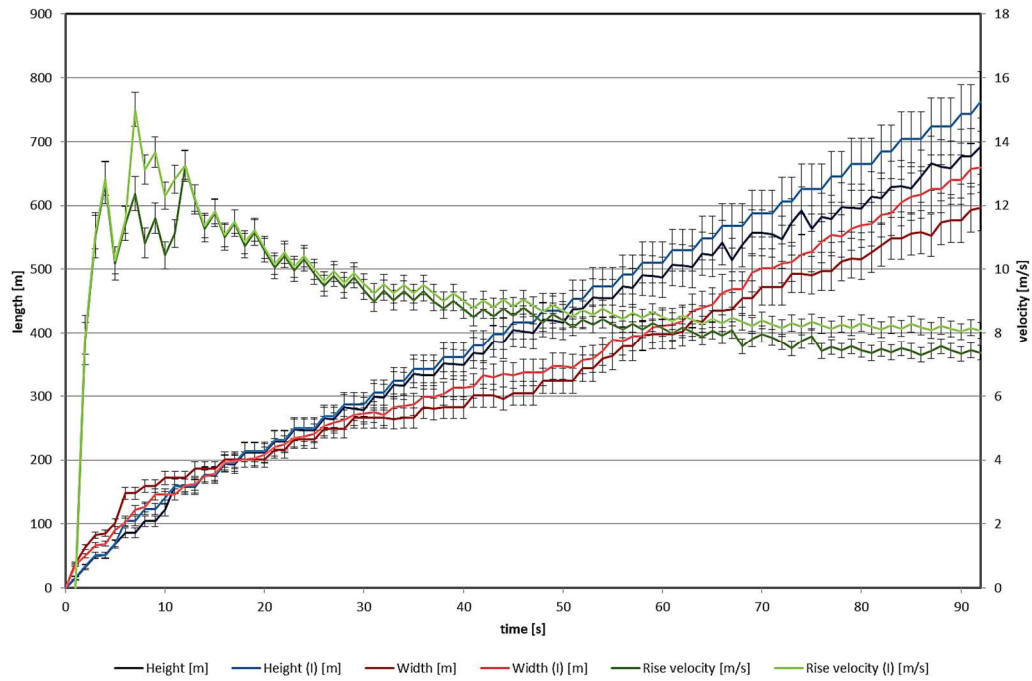
Fig. 4.12: Example of an automatic Excel output, with plume height, width and rise velocity in the wind-corrected plane and image plane (I), and related errorbars (P44 explosion, 10th August 2018).
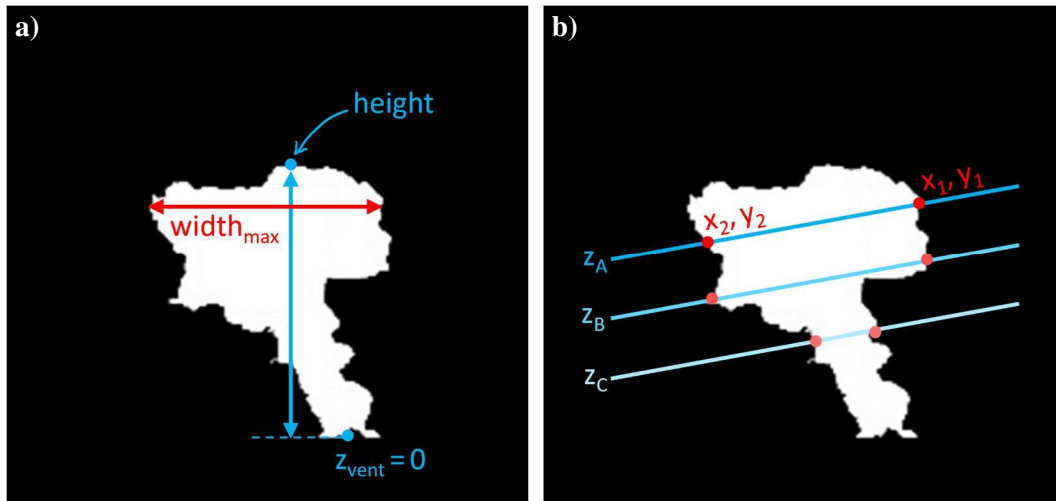

Fig. 4.13: Figures showing (a) where the geometric parameters of the plumes are calculated and (b) a simplified construction explaining how the plume width is calculated in the wind-corrected plane (P31 explosion, 8th August 2018).

5.3.3. Rise velocity

The change in plume height between two frames can be converted to ascent velocity, calculated along the vertical axis, by using the time elapsed between them. The algorithm calculates both an instantaneous and a time-averaged rise velocity. The first is the height difference of the plume in the two consecutive frames divided by the time difference between the two frames. The latter is obtained by dividing the plume height reached in the current frame with the time elapsed since the eruption onset. Also in this case, the ascent velocity is calculated both in the image and in the wind-corrected plane.

5.3.4. Air entrainment

The entrainment coefficient is linked to the height and radius of the plume, that are calculated in the algorithm (the radius is half the width), but differs depending on the plume dynamics. In reality, what has so far been called the vent in in this chapter corresponds to the side of the crater that is visible the camera, as the real emission point is hidden by the crater itself. To solve this issue, the shape of the plume from its base has been extended until the two side lines intersect. Then, by using the known radius at the base and by geometrically calculating the inclination of these lines with respect to the vertical, it is possible to find a virtual depth of the vent (law of sines) that must be added to the height above the crater rim to calculate the air entrainment through Eqs. 4.24-4.26 (Fig. 4.14). It is important to note that the virtual source defined by this method is not expected to be the real location of the vent. Instead, inside the crater, the plume margins are very steeply curved. Moreover, it is also important to stress that this method is applied to a single frame (generally the last one) to understand also the evolution of the internal plume dynamics; this is done by plotting the height versus the entrainment coefficient itself. Another important factor to account for is the inclination of the plume, that may affect the entrainment coefficient calculation. So, only plumes with trajectories near to the vertical and slightly influenced by wind velocity should be considered.

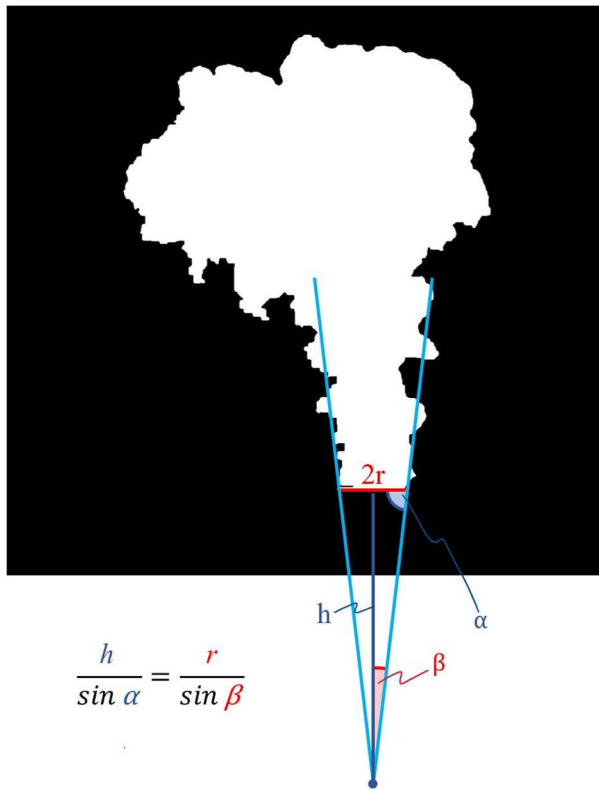$$\frac{h}{\sin \alpha} = \frac{r}{\sin \beta}$$

Fig. 4.14: Geometric calculations to be applied to determine the apparent depth of the vent h. Notice that the plume is almost spreading in the vertical direction (P31 explosion, 8th August 2018).

6. Results & discussion

Before presenting the results of the image analysis, it is helpful to recall that the timescale of Vulcanian eruption duration is usually short compared to the rise time of the resulting eruption plume (Sparks et al., 1997), and is on the order of tens of seconds to a minute at Sabancaya, compared to longer times of rise (1-2 minutes). Simply by a visual observation of the videos analysed in this thesis, it is possible to state that the volcanic plumes at Sabancaya rise into the atmosphere as transient/thermal plumes. In fact, the release of ash and gas has a timescale that is comparable to or less than the time required for the full development of the plume. Therefore, it is expected that momentum effects will be important in the initial stages of plume rise and that, subsequently, the plume will decelerate and buoyancy effects will dominate (Sparks et al., 1997). Observations reported in literature suggest that the transition between these two phases may be characterised by deceleration of the thermal to velocities less than 15 m/s (Patrick, 2007).

In general, an eruption lasting 2 minutes and 48 seconds requires almost 37 minutes and 55 seconds to be analysed with the developed algorithm. It seems to be a very long time compared to the plume ascent time, but as stated before, just by skipping the width calculation in the wind-corrected plane, this time can drop to 24 minutes and 44 seconds. Considering also the laptop specifications, this time could be reduced again by running the algorithm on a more powerful processor.

6.1. Success and limitations of video analysis & calibrations

The first aim of the project was to create a method capable of developing segmented masks for eruption plumes recorded with visible wavelength cameras that exclude noise and provide a good outline of the plume boundaries. This is done well and with promising results by the developed algorithm (Fig. 5.1).

The primary problem related to the use of video recorded in visible wavelengths the fact that each pixel is associated with a true colour resulting from the combination

of the three RGB channels. Furthermore, a strong difference in pixel intensity between the plume and the background is required to obtain a good plume isolation. Thus, the algorithm does not work as well for videos with high cloudy conditions as for those in which there is a higher contrast between the plume and the background (i.e., a blue sky). Sometimes, this situation requires the user to choose between a good reproduction of the plume boundaries with some noise, and a less noisy segmented image where parts of the plume are lost (Fig. 5.2). Therefore, videos in these conditions were not subsequently analysed. Although this represents a limit for the application of the developed algorithm, since meteorological clouds and volcanic degassing are common, 26 out of 49 explosions were recorded in sufficiently good conditions to analyse. Further work to improve the algorithm such that image segmentation under bad background conditions would be one of the main enhancements that could be done in the future. However, it is also important to note that the presence of some clouds does not always negatively affect the image processing since, if they are sufficiently spatially-separated from the plume they can easily be filtered from the final segmented image.

Moreover, the algorithm was also compared to Plume Ascent Tracker (Valade et al., 2014), showing that it works well at detecting a well-contrasted plume in a non-moving, clear background and uniformly lighted environment (Bombrun et al., 2017). In all the other cases, the thresholds that can be set through the user interface are not reliable (Fig. 5.3).

To assess if the geometric calibration is accurate and to verify the code it is useful to compare a known a priori length with that measured in the image. Here, the comparison was made between the diameter of the crater and the basal width of the volcanic plumes. The measured maximum diameter of Sabancaya crater is 384 m (Rivera et al., 2016) which is comparable with the plumes' basal widths as calculated by the algorithm (the greatest value is almost 360 m), confirming that the geometric calibration works well. However, the geometric calibration produces a systematic error associated with the spatial resolution of the image, that must be taken into consideration and is automatically calculated by the algorithm. Another factor that should be considered is the uncertainty associated with the manual

Fig. 5.1: Superimposition of the plume shape tracked by the algorithm on the original image (P31 explosion, 8th August 2018).

Fig. 5.2: Example of a mask generated in cloudy conditions. Parts of the clouds are erroneously identified as plume pixels (P38 explosion, 6th August 2018).
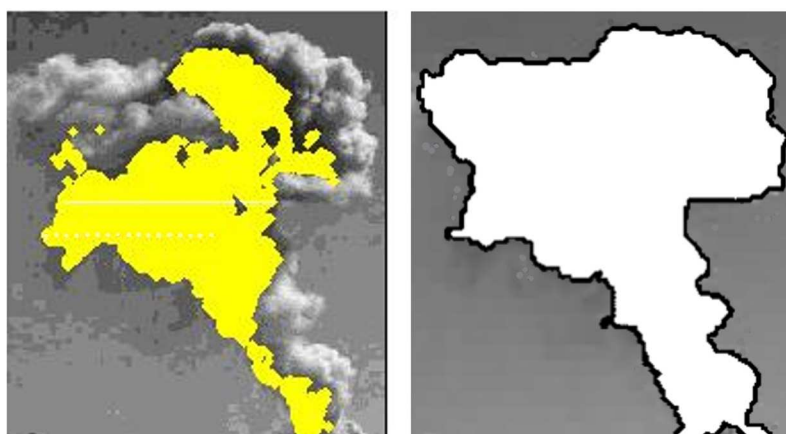

Fig. 5.3: Comparison between plume segmentation obtained with (a) the Plume Ascent Tracker algorithm (Valade et al., 2014) and (b) the algorithm developed here, both applied to the same frame of the same eruption at Sabancaya (P31 explosion, 8th August 2018).

calculation of the FOV of the camera and of the distances of the camera from the vent. In particular, an error in the FOV of the camera may introduce large errors in the calibration. Thus, it is essential to calculate it accurately if it has not been recorded at the time of filming.

Other sources of error during the calibration phase could arise from the wind correction. This includes the fact that the whole correction is based on the ERA5 reanalysis data that, given they are not purely based on observations, are associated with an intrinsic uncertainty. Also, the part of the algorithm that assumes that the wind direction is an average of those calculated at different pressure levels by the ERA5 model can cause errors and bad wind corrections. Nevertheless, the largest error occurs in the case in which the wind direction (independently if it is blowing towards the camera or not) is nearly parallel to the camera orientation. In this case, the image and wind-orientated planes are perpendicular and thus it is impossible to project a point from one to the other. This can only be addressed by simultaneously recording the plume from two different locations, ideally with two cameras oriented towards the plume with a 90° angle difference. In the next section this error will be analysed for both the height and width calculated by the algorithm.

6.2. Geometric parameters of the analysed plumes

It is important to compare the results obtained in this study with similar results already obtained in the literature. A particularly key paper in this field is that of Formenti et al. (2003), who measured the geometric parameters of plumes from Vulcanian explosions at Soufrière Hills Volcano, Montserrat. They chose to only consider plumes with a vertical trajectory within 10° of the vertical. Thus, in this section, only plumes with a vertical or near-vertical spreading direction are considered.

6.2.1. Visual analysis of video footage

Only jets that appear to lie approximately in the vertical plane, based on visual and wind direction inspection, were analysed for their geometric properties. This led to the selection of 8 videos out of the remaining 26 (Table 2). Here follows a short visual description of these explosions:

- P8: The ejection of material lasts about 2 minutes, and the plume develops its shape in the same time span, thus suggesting it behaves as a transient plume. The reached height is not sufficient to develop a clear umbrella shape, so the plume rises vertically into the atmosphere, slightly increasing its radius because of air entrainment. Degassing clouds were present at the onset of the explosion, but these were well-removed by the image analysis algorithm described in Section 4.

- P10: The main explosion lasts about less than 2 minutes and is accompanied by a minor explosion that develops on the side away from the main crater. The relative timescales suggest a transient/thermal behaviour that ends with the formation of an umbrella region in the last part of the recording. Again, low degassing is present.

- P11: Explosion time is estimated at 1 minute and a half, reaching a maximum height lower than the previous plumes, but the timescale still suggests a transient/thermal plume. A small umbrella-shape head develops.

- P1: The explosion lasts more than 2 minutes producing a transient plume with a well-developed umbrella. The presence of a meteorological cloud in the spreading direction which is slowly obscured by the plume is corrected through post-processing of the image analysis.

- P31: This explosion behaves like P1, but it is more influenced by local wind.

- P42: Ejection of volcanic materials lasts about a minute and the consequent plume has a finger-like shape with thermal behaviour. Degassing is present.

- P35: Explosion similar to P42. Degassing was present at the start.

- P44: Explosion time is estimated as 1 minute, producing a transient/thermal plumes similar to P11 in shape. A small umbrella-shape head develops.

Table 2. Shooting features of videos corresponding to selected explosions. From the left, the camera-vent distance Y, the horizontal and vertical FOV β_h and β_v, the camera inclination ϕ and orientation Ω, the wind direction ω and the calculated χ angle.

Explosion	Y (m)	β_h	β_v	ϕ	Ω	ω	χ
P1	20607 ± 171	14.7°	8.3°	4°	256.3 N	52.8 N	66.40°
P10	5520 ± 207	69.3°	39.0°	18°	209.2 N	57.6 N	61.65°
P11	5073 ± 235	64.5°	36.3°	18°	188.5 N	58.2 N	40.35°
P31	5073 ± 235	64.5°	36.3°	18°	188.5 N	58.2 N	40.35°
P35	20607 ± 171	14.7°	8.3°	4°	256.3 N	64.4 N	78.05°
P42	3744 ± 225	63.0°	35.4°	21°	11.4 N	79.9 N	21.50°
P44	3744 ± 225	63.0°	35.4°	21°	11.4 N	86.2 N	15.20°
P8	3744 ± 225	63.0°	35.4°	21°	11.4 N	79.9 N	21.50°

6.2.2. Height

Before proceeding to present quantitative results on the geometric parameters of the selected videos, it is important to evaluate the effect of a wind direction parallel or nearly parallel to the camera orientation on the calculated height of a plume. This condition means that the χ angle is almost 90° and produces a large error in evaluating where the plume actually is, leading to significant scatter in the height data (Fig 5.4a) or to heavily under- or over-estimate the height. This problem also slightly affects the selected dataset, i.e., the P35 explosion (Table 2), for which the wind-uncalibrated height was then considered.

The resulting maximum heights are compatible with the heights of ash plumes reported by the IGP and InGeMMet (Global Volcanism Program, 2018), with plumes rising at least up to 3 km above the vent (Fig. 5.5a & Fig. 5.6a). Depending on the magnitude of the event, plume heads reach heights between 180 and 715 m within 30 seconds after ejection (Table 4 & Fig. 5.6b). The height of plumes as a function of time t can be fitted by a power law $h \propto t^b$, where h is the height of the leading portion of the plume front and b an exponent, that fits to the data with a coefficient of determination higher than 0.99 (Fig. 5.5a & Fig. 5.6a). It has previously been found that $b = 0.5$ for jets and discrete thermals and $b = 0.75$ for starting plumes (Turner, 1962). Table 3 shows the determined values of b along with the associated uncertainty whilst the fitted curves are shown alongside the data in Fig. 5.6. The selected explosions were characterized by a median b of 0.76

(±0.05), which closely matches that expected for the rise of buoyant plumes. Lower values were observed in two plumes (0.56 and 0.69, respectively P10 and P1), probably reflecting initial jet behaviour followed by buoyant plume rise. Moreover, another two plumes showed values greater than one (1.05 for P11 and 1.12 for P35), with rise trends that are close to linear due to different reasons: P11 probably because of the lack of initial momentum and being dominated solely by buoyancy (Patrick, 2007), while P35 is probably an artefact. In fact, P35 should behave more like a jet-phase plume, simply because from the visual analysis it was stated that its behaviour was similar to P42. Furthermore, it is different from P11, that in the recorded video seems to develop vortexes due to entrained air even from the explosion onset. This could be caused by an unproper manual correction of the maximum heights reached by the plume in the first few seconds after the start of the explosion. This correction was necessary because of the presence of volcanic degassing clouds that were recognized as parts of the plume. However, P11 behaviour should be investigated further, even if it really appears to have a purely buoyant pattern.

6.2.3. Width & radius

In most models and previous studies, the horizontal geometric parameter of the plume which is considered is the radius. As plumes are usually modelled as conical bodies, each horizontal slice of this body has a calculated width that can be assumed to be the diameter of the ideal circle represented by the slice (in plane view). Therefore, the half width of the plume will be considered as the radius.

The effect of a wind correction applied to videos in which camera orientation and wind direction are near to parallel, has a huge consequence on the width determination. In fact, the result is exaggerated with respect to that obtained with only the geometric calibration and does not represent a reliable output (Fig. 5.4b). This is the case of the P1, P10 and P35, which width was not well-corrected for the local wind field. Thus, for these explosions the wind-uncalibrated width is considered.

Another problem that can arise concerns the method of calculation of the width itself. The method of determining the line along which all plume pixels have the same height is often a source of error. This happens because it does not consider a line with the same angular coefficient for each pixel starting from the bottom of the image, that would have been the best method to extract the width, but it was computationally expensive. This is the reason why the calculated width of P42 plume has a constant trend in the last plotted 20 s of rise (Fig. 5.5b). This does not reflect the real shape evolution of the plume. However, the results for the remaining 4 selected videos (P11, P31, P44 and P8) are satisfactory: data are not scattered and reflect a similar trend of the wind-uncalibrated width, both for the maximum radius of the plume and for the radius as a function of height in each frame.

Given that curves of the maximum radius as a function of time have a similar shape of those for the height (e.g., Fig. 4.12), the same power law is used to fit to the data (Fig 5.5b & Fig. 5.7). The maximum radii of Sabancaya plumes seem to follow a more linear path then heights, mostly after the first 5 s of the explosion. The qualitative observation made before about the similarity between the P35 and P42 explosions is confirmed here and also supports the conclusion that the fitted power law for the height of the P35 explosion is not compatible with its dynamics. This observation is confirmed also by the top height versus maximum radius plot (Fig. 5.8), where they follow a similar path. For all the other explosions, Fig. 5.8 shows an almost linear relationship between the height of the head and the maximum radius of the plumes while ascending into the atmosphere.

6.3. Rise velocity

Vertical rise velocity is directly calculated from the image as a function of the evolution in time of the maximum height of the plume. However, for these purposes it is easier and more accurate to calculate the velocity as the time-derivative of the height of the plume top, so it is produced from the smoothed height data and follows the law $v = abt^{b-1}$.
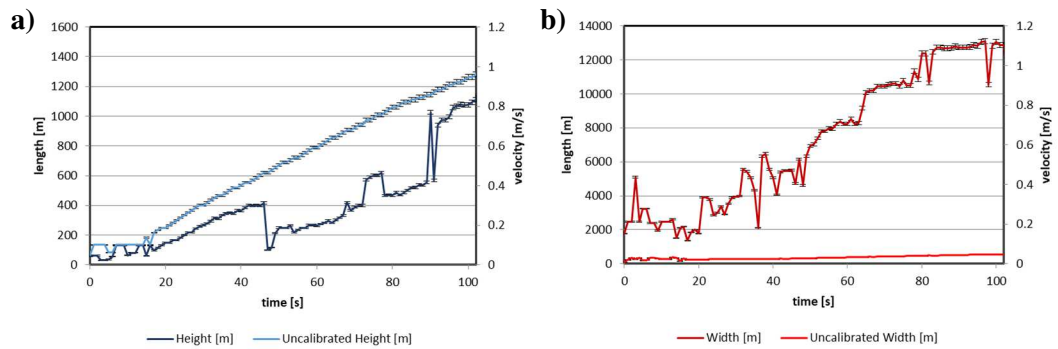
Fig. 5.4: Examples of distorted (a) height and (b) width calculations, because of the effect of wind correction in a context of almost parallel camera orientation (253.7°) and wind direction (80°) (P5a explosion, 11th August 2018).
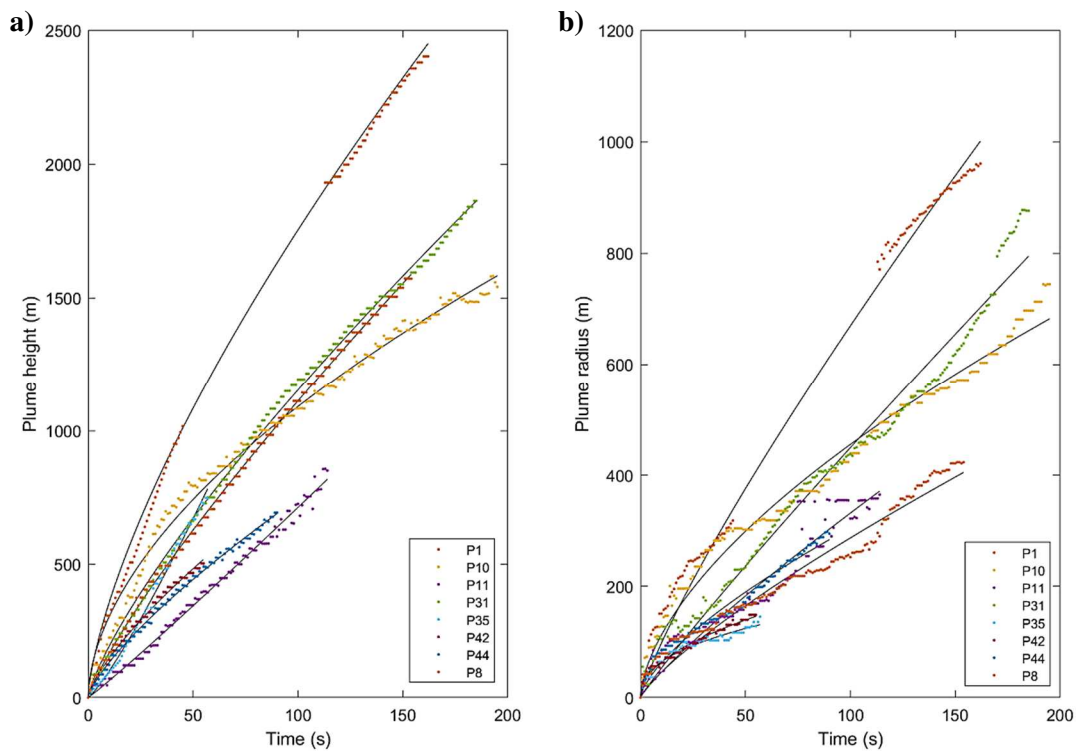

Fig. 5.5: Plot of raw data of (a) height of the top of the plume and (b) maximum radius of the plume, both as a function of time after the start of the explosion. The black lines are the power low fits based on the dependence proposed by Turner (1962).

Table 3. Power law for height versus time ($h = at^b$) with associated standard deviation (2σ) and coefficient of determination (R^2).

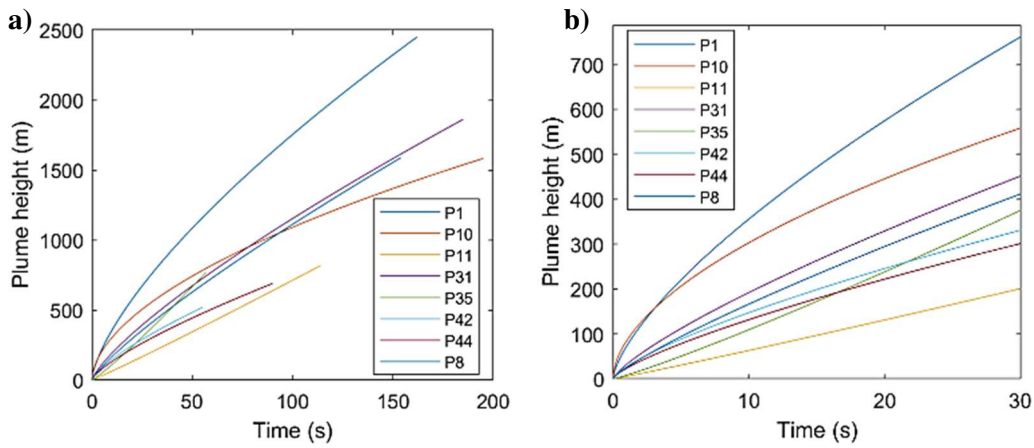| Explosion	b	2σ	R²
P1	0.69	0.01	0.9962
P10	0.56	0.01	0.9913
P11	1.05	0.02	0.9936
P31	0.78	0.01	0.9978
P35	1.12	0.05	0.9953
P42	0.74	0.02	0.9940
P44	0.75	0.01	0.9974
P8	0.82	0.01	0.9991

Fig. 5.6: Height of the top of the plume versus time for (a) the whole duration of the explosions and (b) within 30 seconds from the explosion onset. Data are smoothed by resampling basing on the best power law fit.
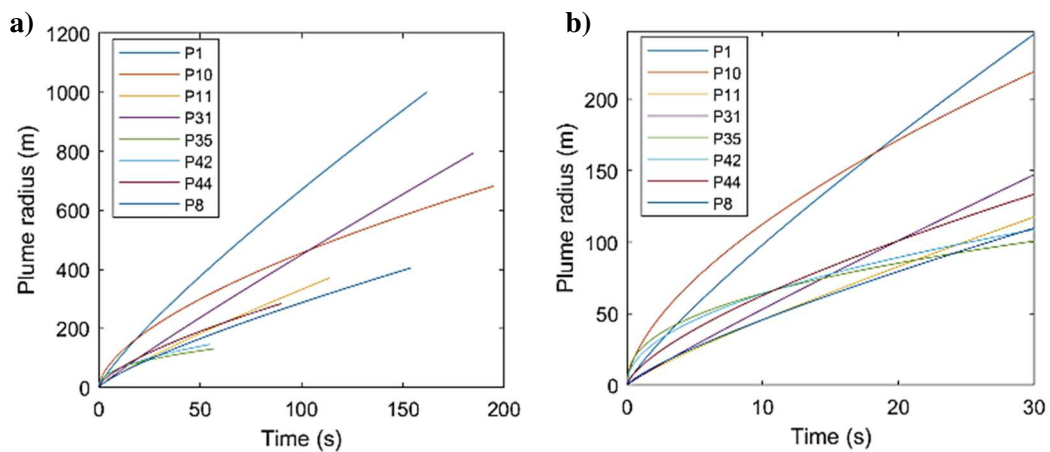

Fig. 5.7: Maximum radius of the plume versus time for (a) the whole duration of the explosions and (b) within 30 seconds from the explosion onset. Data are smoothed by resampling basing on a power law fit similar to that of height.
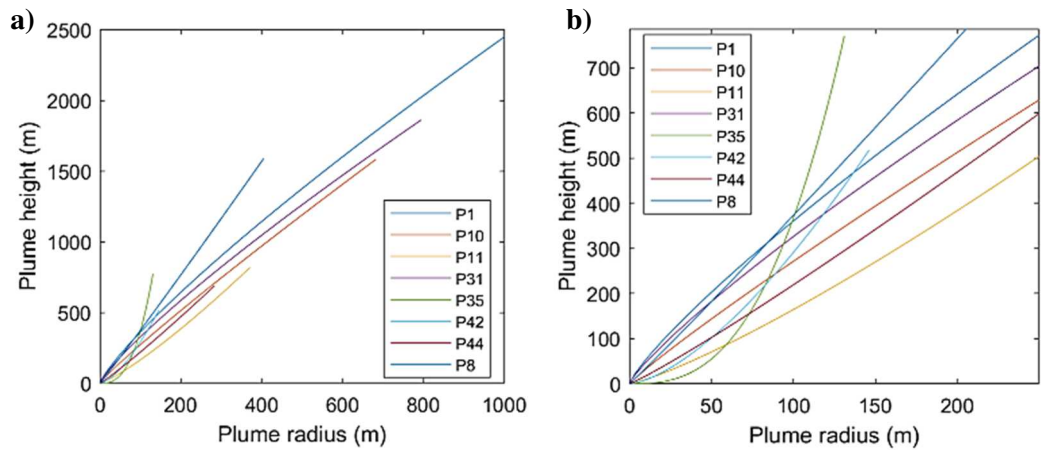
62

Fig. 5.8: Height of the leading portion of the plume versus maximum radius for (a) the whole duration of the explosions and (b) within 30 seconds from the explosion onset.
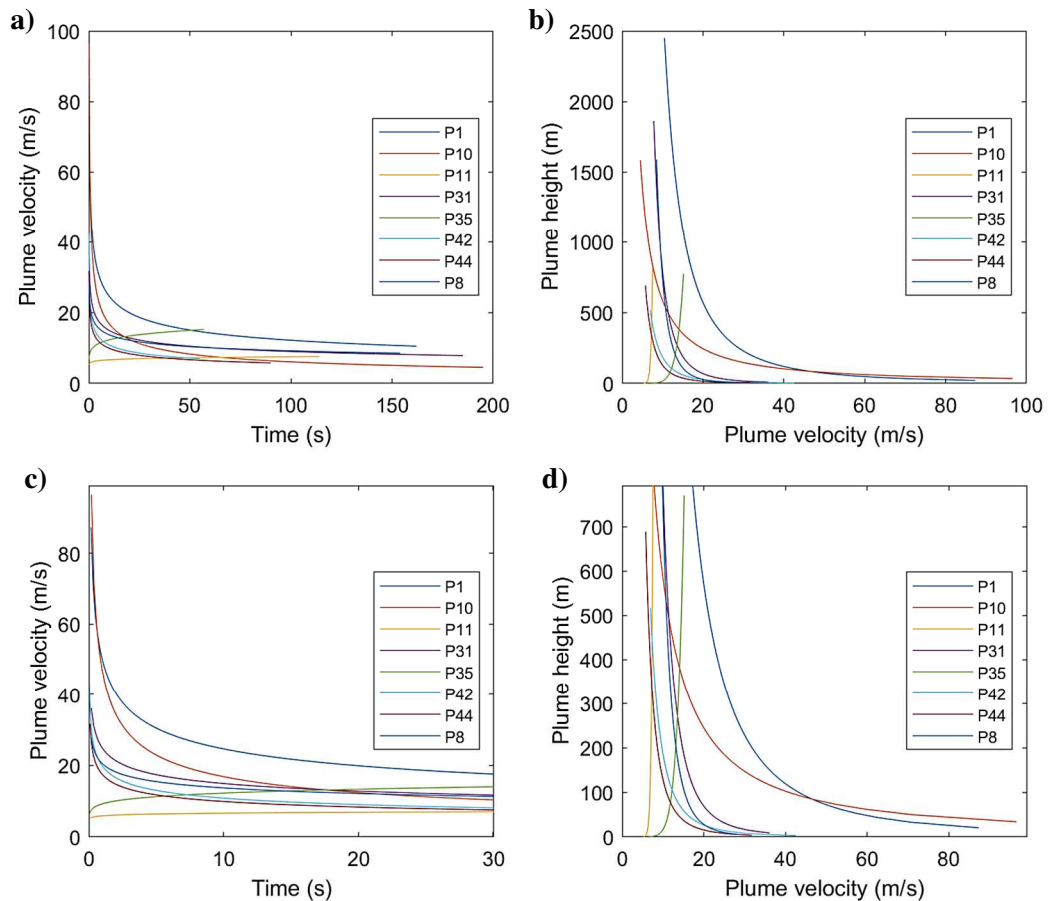

Fig. 5.9: Graphs showing the evolution of vertical ascent velocity of the leading part of the plume as a function of (a-c) time and (b-d) height of the head (where velocity is measured), for (a-b) the whole duration of the explosions and (c-d) within 30 seconds from the explosion onset.

The results of the calculation (Fig. 5.9) demonstrate that the rise velocity of the plume head reflects two different phases described on the basis of the plume morphology (Tournigand et al., 2017). These are the initial momentum-dominated gas-thrust phase and the subsequent buoyancy-driven phase, in which entrained air and temperature play important roles (Patrick, 2007; Patrick et al., 2007). During the gas-thrust phase, the rise velocity falls rapidly because of the dissipation of the initial momentum, while during the buoyancy phase the rise velocity remains almost constant (continues to decrease, but slowly). The transition between the two velocity phases is often abrupt and occurs 2 to 10 s after the beginning of the explosion. Nevertheless, some plumes show different behaviour, starting with a certain velocity and maintaining it for the whole explosion duration. In this case, the plume is considered initially fully-buoyant and the initial gas-thrust phase is not present. This is the case for the P11 explosion, in which the initial velocity is almost constant with time (only increasing from 5.3 to 7.5 m/s), but not for P35, which, as has already been stated, has a behaviour more similar to the P42 explosion. For the other explosions, the maximum plume rise velocity, attained at the explosion onset, is 96.5 m/s (average is 53.7 m/s; Table 4), while average buoyant rise velocities are between 5 and 15 m/s.

6.4. Air entrainment

To determine the entrainment coefficient for the starting plume phase (without the umbrella region influence) it is necessary to consider the radius as a function of height from a frame taken at a certain time when the umbrella was not developed yet, or from the last image of the plume. The gradient of the lower part of the plume (below the umbrella) is then calculated.

Although Turner (1962) noted that the steady plume and the plume front of starting plumes must be regarded as two separate dynamic entities, since the plume front can entrain air at a much greater rate than the steady plume (Patrick, 2007), the air

Table 4. List of the height of the head, maximum radius and velocity of the head of the plume after 30 s from the start of the explosions, then initial rise velocities and air entrainment coefficients, for the selected explosions. Initial rise velocities are calculated from the fitted curves, that are more reliable.

Explosion	Height (t=30 s) (m)	Radius (t=30 s) (m)	Initial rise velocity (m/s)	Rise velocity (t=30 s) (m/s)	Air entrainment
P1	705.8 ± 7.2	258.9 ± 2.2	87.3	22.8 ± 0.1	0.14
P10	557.3 ± 29.0	252.9 ± 11.7	96.5	18.0 ± 0.5	0.19
P11	192.6 ± 12.0	127.1 ± 5.9	5.3	6.2 ± 0.2	0.18
P31	417.7 ± 4.9	180.0 ± 1.5	36.1	13.5 ± 0.1	0.15
P35	335.8 ± 22.4	102.8 ± 6.2	4.5	10.8 ± 0.4	0.11
P42	320.0 ± 21.5	106.9 ± 6.4	42.5	10.3 ± 0.3	0.16
P44	278.6 ± 19.0	133.0 ± 8.0	31.7	9.0 ± 0.3	0.15
P8	433.7 ± 18.1	119.2 ± 4.5	28.4	14.0 ± 0.3	0.14

entrainment coefficient here was evaluated for the entire plume when the values of the gradient were almost similar along the whole height. The calculated entrainment coefficients (Table 4) are consistent with values stated in literature which, for the steady part of the plume (that below the umbrella region), can range from 0.07 (Patrick, 2007) to 0.30 (Bombrun et al., 2018). It is important to note, however, that the values calculated in this work are lower than values typically observed in laboratory experiments (0.25) (Scorer, 1979).

6.5. Discussion on plume dynamics

The results show that the selected explosions at Sabancaya represent different types of transient plume ascent dynamics or at least its different development stages. Values of the height and velocity of the plume head with time are consistent with other observed eruptions in the world. In fact, Vulcanian plumes at Soufrière Hills and Sakurajima volcanoes exhibit similar trends (Formenti et al., 2003; Tournigand et al., 2017) to the results here presented. Even though Vulcanian and Strombolian eruptive styles may differ in several aspects, Tournigand et al. (2017) showed that initial plume dynamics from both styles share many common features. In both cases the impulsive, unsteady nature of the eruption mechanism strongly controls the features and evolution of the resulting transient plumes. This is the reason why the

trajectories of volcanic plumes at Sabancaya also resembles those of Strombolian eruptions (Patrick et al., 2007; Tournigand et al., 2017; Bombrun et al., 2018). However, Vulcanian plumes rise differently due to variations in initial velocity, and can begin with a gas-thrust phase that decays into a roughly linear rise with height. This results in a power law dependence, $h \propto t^b$, assuming values similar to those associated to starting plumes (Turner, 1962). Even though it has been calculated slightly differently, the air entrainment coefficient was also similar to other values in the literature for transient plumes (Patrick, 2007; Bombrun et al., 2018).

7. Conclusions

Volcanic plumes are dangerous ejections of volcanic gas and tephra that can cause fallout over large areas causing widespread health issues as well as structural damage to buildings and troubles to aviation. The presented algorithm allowed, through the analysis of high-resolution videos, parameterization of the evolution of Vulcanian-style eruptive plumes at Sabancaya volcano, Peru, in terms of their morphology, rise velocity and air entrainment. The algorithm developed to identify plume-containing pixels is new and is hopefully of significant use to the wide volcanological community.

This point has already been stressed, but the main advantages of using videos recorded in the visible wavelengths are in terms of the costs of the camera and resolution of the final output. However, quantitative analysis of visible images of volcanic plumes has almost always been overlooked, because of the difficulty in obtaining a clean plume tracking. This work confirms that this type of image processing is possible, especially if applied in good weather conditions. However, further work should focus on improving the algorithm to track plumes for a wider range of meteorological conditions and to enhance the width calculation.

The application of the algorithm to Sabancaya case study pointed out that these volcanic plumes are mainly characterized by a transient/thermal behaviour. In particular, the calculated heights were fitted by a power law ($h \propto t^b$) and the median of the b value (0.76 ±0.05) suggests that Vulcanian plumes at Sabancaya rise as buoyant plumes (Turner, 1962). However, the derived rise velocity of the plume head with time reflects the presence of a momentum-dominated gas-thrust phase (high ejection velocity that rapidly drops), followed by a buoyancy-driven phase (almost constant rise velocity) (Patrick, 2007; Patrick et al., 2007). This two-phase pattern is also suggested by two plume heights modelled with a lower value of b (Turner, 1962). Another particular case is represented by a probably fully-buoyant plume, in which the height is increasing almost linearly with time and the rise velocity is nearly constant from the onset of the explosion. The algorithm

calculated also the width of the plume, from which the maximum radius and the radius as a function of height as a function of time were obtained. Apart from the supposed fully-buoyant explosion, the maximum radius is characterized by a quite linear relationship with the height of the head of the plumes while ascending into the atmosphere. On the other hand, the radius of the plume as a function of height was used to estimate the air entrainment coefficients, that resulted to be consistent with values stated in literature (Patrick, 2007; Bombrun et al., 2018).

Considering current computers specifications and speeds, the algorithm could be potentially applied to nearly real time monitoring and forecasting and may reveal even more dynamical information. This could be done by adding new section to the main script, thus applying different models (e.g., Woods & Kienle, 1994; see Appendix A) or equations (Tournigand et al., 2017; Valade et al., 2014; Yamamoto et al., 2008; Formenti, 2003) from the literature that could enable important parameters about volcanic plumes, such as the mass (Bonadonna et al., 2002), the volume or the ash mass of the plume (Tournigand et al., 2017), to be inferred. In other words, this algorithm represents an example of how the remote analysis of volcanic plumes can be an essential tool for understanding their dynamics and related hazards. Therefore, given the increasing availability and development of remote-imaging instruments, automated plume detection will play an important role in monitoring or research about volcanic plumes.

References

Boixart, G., Cruz, L.F., Miranda Cruz, R., Euillades, P.A., Euillades, L.D., Battaglia, M., 2020. Source Model for Sabancaya Volcano Constrained by DInSAR and GNSS Surface Deformation Observation. Remote Sensing 12, 1852. https://doi.org/10.3390/rs12111852

Bombrun, M., Jessop, D., Harris, A., Barra, V., 2018. An algorithm for the detection and characterisation of volcanic plumes using thermal camera imagery. Journal of Volcanology and Geothermal Research 352, 26–37. https://doi.org/10.1016/j.jvolgeores.2018.01.006

Bonadonna, C., Macedonio, G., Sparks, R.S.J., 2002. Numerical modelling of tephra fallout associated with dome collapses and Vulcanian explosions: application to hazard assessment on Montserrat. Geological Society, London, Memoirs 21, 517–537. https://doi.org/10.1144/GSL.MEM.2002.021.01.23

Chojnicki, K.N., Clarke, A.B., Phillips, J.C., Adrian, R.J., 2015. The evolution of volcanic plume morphology in short-lived eruptions. Geology 43, 707–710. https://doi.org/10.1130/G36642.1

Clarke, A.B., Voight, B., Neri, A., Macedonio, G., 2002. Transient dynamics of vulcanian explosions and column collapse. Nature 415, 897–901. https://doi.org/10.1038/415897a

Faccenna, C., Oncken, O., Holt, A.F., Becker, T.W., 2017. Initiation of the Andean orogeny by lower mantle subduction. Earth and Planetary Science Letters 463, 189–201. https://doi.org/10.1016/j.epsl.2017.01.041

Gerbe, M.-C., Thouret, J.-C., 2004. Role of magma mixing in the petrogenesis of tephra erupted during the 1990–98 explosive activity of Nevado Sabancaya, southern Peru. Bull Volcanol 66, 541–561. https://doi.org/10.1007/s00445-004-0340-3

Global Volcanism Program, 2017. Report on Sabancaya (Peru) (Crafford, A.E., and Venzke, E., eds.). Bulletin of the Global Volcanism Network, 42:5. Smithsonian Institution. https://volcano.si.edu/ShowReport.cfm?doi=10.5479/si.GVP.BGVN201705-354006 (accessed 6.26.21).

Global Volcanism Program, 2018. Report on Sabancaya (Peru). In: Sennert, S K (ed.), Weekly Volcanic Activity Report, 1 August-7 August 2018. Smithsonian Institution and US Geological Survey. https://volcano.si.edu/ShowReport.cfm?doi=10.5479/si.GVP.WVAR20180801-354006 (accessed 6.26.21).

Global Volcanism Program, 2018. Report on Sabancaya (Peru). In: Sennert, S K (ed.), Weekly Volcanic Activity Report, 8 August-14 August 2018. Smithsonian Institution and US Geological Survey. https://volcano.si.edu/ShowReport.cfm?doi=10.5479/si.GVP.WVAR20180808-354006 (accessed 6.26.21).

Global Volcanism Program, 2018. Report on Sabancaya (Peru). In: Sennert, S K (ed.), Weekly Volcanic Activity Report, 25 July-31 July 2018. Smithsonian Institution and US Geological Survey. https://volcano.si.edu/ShowReport.cfm?doi=10.5479/si.GVP.WVAR20180725-354006 (accessed 6.26.21).

Global Volcanism Program, 2018. Report on Sabancaya (Peru) (Krippner, J.B., and Venzke, E., eds.). Bulletin of the Global Volcanism Network, 43:12. Smithsonian Institution. https://volcano.si.edu/ShowReport.cfm?doi=10.5479/si.GVP.BGVN201812-354006 (accessed 6.26.21).

Global Volcanism Program, 2021. Report on Sabancaya (Peru). In: Sennert, S K (ed.), Weekly Volcanic Activity Report, 16 June-22 June 2021. Smithsonian Institution and US Geological Survey. https://volcano.si.edu/ShowReport.cfm?doi=10.5479/si.GVP.WVAR20210616-354006 (accessed 6.26.21).

Hersbach, H., Bell, B., Berrisford, P., Biavati, G., Horányi, A., Muñoz Sabater, J., Nicolas, J., Peubey, C., Radu, R., Rozum, I., Schepers, D., Simmons, A., Soci, C., Dee, D., Thépaut, J.-N., 2018. ERA5 hourly data on pressure levels from 1979 to present. Copernicus Climate Change Service (C3S) Climate Data Store (CDS). (Accessed on 27-Apr-2021), https://doi.org/10.24381/cds.bd0915c6

Jay, J.A., Delgado, F.J., Torres, J.L., Pritchard, M.E., Macedo, O., Aguilar, V., 2015. Deformation and seismicity near Sabancaya volcano, southern Peru, from 2002 to 2015. Geophysical Research Letters 42, 2780–2788. https://doi.org/10.1002/2015GL063589

Kern, C., Masias, P., Apaza, F., Reath, K.A., Platt, U., 2017. Remote measurement of high preeruptive water vapor emissions at Sabancaya volcano by passive differential optical absorption spectroscopy. Journal of Geophysical Research: Solid Earth 122, 3540–3564. https://doi.org/10.1002/2017JB014020

Lim, H., Kim, Y., Clayton, R.W., Thurber, C.H., 2018. Seismicity and structure of Nazca Plate subduction zone in southern Peru. Earth and Planetary Science Letters 498, 334–347. https://doi.org/10.1016/j.epsl.2018.07.014

MacQueen, P., Delgado, F., Reath, K., Pritchard, M.E., Bagnardi, M., Milillo, P., Lundgren, P., Macedo, O., Aguilar, V., Ortega, M., Anccasi, R., Zerpa, I.A.L., Miranda, R., 2020. Volcano-Tectonic Interactions at Sabancaya Volcano, Peru: Eruptions, Magmatic Inflation, Moderate Earthquakes, and Fault Creep. Journal of Geophysical Research: Solid Earth 125, e2019JB019281. https://doi.org/10.1029/2019JB019281

Manea, V.C., Manea, M., Ferrari, L., Orozco-Esquivel, T., Valenzuela, R.W., Husker, A., Kostoglodov, V., 2017. A review of the geodynamic evolution of flat

slab subduction in Mexico, Peru, and Chile. Tectonophysics 695, 27–52. https://doi.org/10.1016/j.tecto.2016.11.037

Manrique Llerena, N., Lazarte Zerpa, I.A., Cueva Sandoval, K.A., Rivera Porras, M.A., Aguilar Contreras, R., 2018. Actividad del volcán Sabancaya (Perú) 2016-2017: Características de las emisiones de ceniza y análisis granulométrico. Instituto Geológico, Minero y Metalúrgico – INGEMMET.

Mariño Salazar, J., Rivera Porras, M.A., Samaniego Eguiguren, P., Macedo Franco, L.D., 2016. Evaluación y zonificación de peligros volcán Sabancaya, región Arequipa. Instituto Geológico, Minero y Metalúrgico – INGEMMET.

Morton, B.R., Taylor, G., Turner, J.S., 1956. Turbulent Gravitational Convection from Maintained and Instantaneous Sources. Proceedings of the Royal Society of London Series A 234, 1–23. https://doi.org/10.1098/rspa.1956.0011

Moussallam, Y., Tamburello, G., Peters, N., Apaza, F., Schipper, C.I., Curtis, A., Aiuppa, A., Masias, P., Boichu, M., Bauduin, S., Barnie, T., Bani, P., Giudice, G., Moussallam, M., 2017. Volcanic gas emissions and degassing dynamics at Ubinas and Sabancaya volcanoes; implications for the volatile budget of the central volcanic zone. Journal of Volcanology and Geothermal Research 343, 181–191. https://doi.org/10.1016/j.jvolgeores.2017.06.027

Patrick, M.R., 2007. Dynamics of Strombolian ash plumes from thermal video: Motion, morphology, and air entrainment. Journal of Geophysical Research: Solid Earth 112. https://doi.org/10.1029/2006JB004387

Patrick, M.R., Harris, A.J.L., Ripepe, M., Dehn, J., Rothery, D.A., Calvari, S., 2007. Strombolian explosive styles and source conditions: insights from thermal (FLIR) video. Bull Volcanol 69, 769–784. https://doi.org/10.1007/s00445-006-0107-0

Pritchard, M.E., Simons, M., 2004. An InSAR-based survey of volcanic deformation in the central Andes. Geochemistry, Geophysics, Geosystems 5. https://doi.org/10.1029/2003GC000610

Puma Sacsi, N., Torres Aguilar, J.L., 2020. Evaluación y análisis de la actividad sísmica en el volcán Sabancaya, periodo 1990-2019. Instituto Geofísico del Perú - Informe vulcanológico.

Puma Sacsi, N., Torres, J.L., Macedo, O., Centeno, R., Del Carpio, J., Cruz, J., 2016. Evolución de la actividad sismo-volcánica en la zona del volcán sabancaya (2013-2016). XVIII Congreso Peruano de Geología.

Rivera Porras, M.A., Mariño Salazar, J., Samaniego Eguiguren, P., Delgado Ramos, R., Manrique Llerena, N., 2016. Geología y evaluación de peligros del complejo volcánico Ampato - Sabancaya, Arequipa - [Boletín C 61]. Instituto Geológico, Minero y Metalúrgico - INGEMMET.

Samaniego, P., Rivera, M., Mariño, J., Guillou, H., Liorzou, C., Zerathe, S., Delgado, R., Valderrama, P., Scao, V., 2016. The eruptive chronology of the Ampato–Sabancaya volcanic complex (Southern Peru). Journal of Volcanology and Geothermal Research 323, 110–128. https://doi.org/10.1016/j.jvolgeores.2016.04.038

Schneider, C.A., Rasband, W.S., Eliceiri, K.W., 2012. NIH Image to ImageJ: 25 years of image analysis. Nat Methods 9, 671–675. https://doi.org/10.1038/nmeth.2089

Scorer, R.S., 1980. Buoyancy effects in fluids. By J. S. Turner. Cambridge University Press Paperback. £7.95. 1979. pp. 368 + xvi. Quarterly Journal of the Royal Meteorological Society 106, 900–901. https://doi.org/10.1002/qj.49710645020

Sigurdsson, H., Houghton, B.F., McNutt, S.R., Rymer, H., Stix, J. (Eds.), 2015. The encyclopedia of volcanoes, Second edition. ed. Elsevier/AP, Academic Press is an imprint of Elsevier, Amsterdam; Boston.

Sparks, R.S.J. (Ed.), 1997. Volcanic plumes. Wiley, Chichester; New York.

Stern, C.R., 2004. Active Andean volcanism: its geologic and tectonic setting. Revista geológica de Chile 31, 161–206. https://doi.org/10.4067/S0716-02082004000200001

Tournigand, P.-Y., Taddeucci, J., Gaudin, D., Fernández, J.J.P., Bello, E.D., Scarlato, P., Kueppers, U., Sesterhenn, J., Yokoo, A., 2017. The Initial Development of Transient Volcanic Plumes as a Function of Source Conditions. Journal of Geophysical Research: Solid Earth 122, 9784–9803. https://doi.org/10.1002/2017JB014907

Turner, J.S., 1969. Buoyant Plumes and Thermals. Annual Review of Fluid Mechanics 1, 29–44. https://doi.org/10.1146/annurev.fl.01.010169.000333

Turner, J.S., 1962. The 'starting plume' in neutral surroundings. Journal of Fluid Mechanics 13, 356–368. https://doi.org/10.1017/S0022112062000762

Valade, S.A., Harris, A.J.L., Cerminara, M., 2014. Plume Ascent Tracker: Interactive Matlab software for analysis of ascending plumes in image data. Computers & Geosciences 66, 132–144. https://doi.org/10.1016/j.cageo.2013.12.015

White, R., McCausland, W., 2016. Volcano-tectonic earthquakes: A new tool for estimating intrusive volumes and forecasting eruptions. Journal of Volcanology and Geothermal Research 309, 139–155. https://doi.org/10.1016/j.jvolgeores.2015.10.020

Wilson, L., Sparks, R.S.J., Huang, T.C., Watkins, N.D., 1978. The control of volcanic column heights by eruption energetics and dynamics. Journal of Geophysical Research: Solid Earth 83, 1829–1836. https://doi.org/10.1029/JB083iB04p01829

Woods, A.W., Kienle, J., 1994. The dynamics and thermodynamics of volcanic clouds: Theory and observations from the april 15 and april 21, 1990 eruptions of redoubt volcano, Alaska. Journal of Volcanology and Geothermal Research 62, 273–299. https://doi.org/10.1016/0377-0273(94)90037-X

Yamamoto, H., Watson, I.M., Phillips, J.C., Bluth, G.J., 2008. Rise dynamics and relative ash distribution in vulcanian eruption plumes at Santiaguito Volcano, Guatemala, revealed using an ultraviolet imaging camera. Geophys. Res. Lett. 35, L08314. https://doi.org/10.1029/2007GL032008

Appendix

A. Woods & Kienle's thermal model (1994)

The developed algorithm is also set to start an inversion with the model of Woods & Kienle (1994), even if it is not tuned at the moment; however, the process cannot be fully-automatic, as the plumes should be chosen by the user to avoid weak plumes or oblique-spreading plumes. This model can represent the basis from which eruptive source parameters (e.g., erupted mass) are inferred, as its outputs can be represented by the density of the plume, the temperature or the gas mass fraction.

The model developed by Woods & Kienle (1994) analyses the ascent of a co-ignimbrite plume as a discrete thermal and applies to situations in which buoyant material is separated by suspension from a hot ash flow, on a timescale which is short compared to the ascent time of the material in the atmosphere. Given this incipit, this model is also suitable for thermal to transient plumes, like Vulcanian-type ones. As the plume ascends into the atmosphere, it entrains and heats the surrounding air; so, its bulk density decreases below that of the atmosphere and becomes more buoyant. Therefore, the plume front speeds up until the force required to displace the air ahead of the cloud exceeds the buoyancy force, producing the umbrella region. As the observed shape suggests, the plume is modelled as a sphere that entrains air through vortexes, at a rate proportional to the upward velocity. The equations that describe the model are:

$$\frac{d}{dt}(r^3\beta) = 3r^2\alpha\varepsilon w \tag{3.1}$$

$$\frac{d}{dt}(r^3(2\beta + \alpha)w) = 2g(\alpha - \beta)r^3 \tag{3.2}$$

$$\frac{d}{dt}\left(r^3\beta\left(C_p\theta + gh + \frac{w^2}{2}\right)\right) = 3r^2\alpha\varepsilon w(C_a\theta_e + gh) \tag{3.3}$$

where ε is the air entrainment constant, h the maximum height, w the vertical rise velocity, r the radius, β the density, θ the temperature and C_p the mass-averaged

specific heat related to the plume (considering those for air, solid particles, vapor, volcanic volatiles and water), while α is the density, θ_e the temperature and C_a the specific heat of the entrained atmospheric air; g is the gravitational acceleration. Going into more detail, these equations represent the conservation of mass (Eq. 3.1), of momentum (Eq. 3.2) and of enthalpy (Eq. 3.3) of the plume. Eq. 3.1 considers the variation of mass due to the entraining of air into a spheric plume with a certain density and ascending in the atmosphere with a certain velocity; Eq. 3.2 evaluates the momentum, considering the addition of mass due to the entrained air (practically, describes the forces that act on the ash cloud, thus buoyancy and the resistance opposed by atmospheric air); Eq. 3.3 is the variation of energy of the plume, as air with a certain temperature is added at a certain height. These differential equations can be solved applying the equation for density of the ash-gas system in the cloud (Eq. 3.4) and the equation for the conservation of ash (Eq. 3.5), that is assumed to be convected into the atmosphere (thus, not subjected to fallout):

$$\frac{1}{\beta} = \frac{1-n}{\sigma} + \frac{nR\theta}{P} \tag{3.4}$$

$$(1 - n_0)r_0^3\beta_0 = (1 - n)r^3\beta \tag{3.5}$$

where n is the gas mass fraction in the atmosphere, σ the density of the solid particles constituting the plume, R the mass-averaged gas constant for the cloud (considering those for air, vapor and volcanic volatiles), P the atmospheric pressure and variables with subscript-zero are referred to a previous time. Their model showed that the height of rise of thermals depends on the initial thermal energy, atmospheric stratification and temperatures.